INL/RPT-23-72860

Modeling of Prismatic High Temperature Reactors in Pronghorn

May 2023

Nuclear Energy Advanced Modeling and Simulation M3 Milestone

Mauricio Tano[1], Vasileios Kyriakopoulos[1], and Sebastian Schunert[1]

[1] *Idaho National Laboratory*

INL is a U.S. Department of Energy National Laboratory
operated by Battelle Energy Alliance, LLC

DISCLAIMER

This information was prepared as an account of work sponsored by an agency of the U.S. Government. Neither the U.S. Government nor any agency thereof, nor any of their employees, makes any warranty, expressed or implied, or assumes any legal liability or responsibility for the accuracy, completeness, or usefulness, of any information, apparatus, product, or process disclosed, or represents that its use would not infringe privately owned rights. References herein to any specific commercial product, process, or service by trade name, trademark, manufacturer, or otherwise, does not necessarily constitute or imply its endorsement, recommendation, or favoring by the U.S. Government or any agency thereof. The views and opinions of authors expressed herein do not necessarily state or reflect those of the U.S. Government or any agency thereof.

INL/RPT-23-72860

Modeling of Prismatic High Temperature Reactors in Pronghorn

Nuclear Energy Advanced Modeling and Simulation M3 Milestone

Mauricio Tano[1], Vasileios Kyriakopoulos[1], and Sebastian Schunert[1]

[1]Idaho National Laboratory

May 2023

Idaho National Laboratory
Idaho Falls, Idaho 83415

http://www.inl.gov

Prepared for the
U.S. Department of Energy
Office of _________
Under DOE Idaho Operations Office
Contract DE-AC07-05ID14517

Page intentionally left blank

ABSTRACT

Pronghorn is a Multiphysics Object-Oriented Simulation Environment (MOOSE) based thermal-hydraulics code developed at Idaho National Laboratory (INL) for advanced reactor analysis. It has been previously applied to model pebble-bed High Temperature Reactors (HTRs)s, Liquid-Metal Cooled Reactors, and Molten Salt Reactors, among others. This work leverages the coarse-mesh thermal hydraulics capabilities in Pronghorn to model a prismatic-core HTR, namely the Oregon State University (OSU)'s High Temperature Test Facility (HTTF). The HTTF is a 1:4 height scaled-down facility of General Atomics' Modular High Temperature Gas-cooled Reactor. This report summarizes the following results obtained with Pronghorn:

- Verification of the implementation of Churchill's pressure drop in channels against analytical calculations.
- Verification of the energy-porosity formulation in Pronghorn for expected temperature rise across a heated assembly.
- Study of the mesh convergence for the weakly-compressible flow formulation in Pronghorn for a heated fuel assembly.
- Demonstration of a 3D model simulation of the full HTTF core using Pronghorn.

Page intentionally left blank

CONTENTS

ABSTRACT iii

1 Introduction 1

2 Codes and Code Jargon 5

3 Theory 8

3.1 Porous Media Approach to prismatic fuel HTR 8

4 Verification of porous media implementation 12

4.1 Test 1: Verification of Friction Factors in Steady-State, Isothermal Conditions 13

4.2 Test 2: Verification of Enthalpy Balance 14

4.3 Test 3: Grid Convergence Analyses for Fluid Flow 17

4.4 Test 4: Grid Convergence Analyses for the Thermal Conduction Problem. 20

4.5 Test 5: Verification of the Coupled Fluid-Solid Convection Problem. 23

4.6 Test 6: Grid Convergence Analyses for the Conjugated Heat Transfer. 26

5 Model of Oregon State University's High Temperature Test Facility 30

5.1 HTTF Steady State Conditions. 30

5.2 HTTF Transient prior to PG-26 41

6 Summary 46

REFERENCES 48

FIGURES

Figure 1. HTTF geometry. 3
Figure 2. Geometry, temperature profiles, and computational mesh for Test 2.......... 16
Figure 3. Measured thermophysical properties for Greecast 94-F [1]. 21
Figure 4. Geometry, temperature profiles, and computational mesh for Test 4.......... 22
Figure 5. Geometrical representation of the modeled geometry in Test 5. 24
Figure 6. Test 5: verification exercise for heat exchange coefficients. 26
Figure 7. Main flow components modeled in the HTTF. 31
Figure 8. Radial distribution of components modeled in the HTTF.......... 31
Figure 9. Hexagonal homogenization of the core of the HTTF (adapted from HTTF blueprints). 32
Figure 10. Distribution of homogenized assemblies in the core region of the HTTF. 34
Figure 11. Porosity field for the HTTF facility model. 35
Figure 12. Computational mesh used for the HTTF model. 36
Figure 13. Results for the velocity field in the best-estimate steady-state boundary conditions for the HTTF. 38
Figure 14. Results for the pressure and power source in the best-estimate steady-state boundary conditions for the HTTF.......... 39
Figure 15. Results for the fluid temperature profiles for different thermal conductivity homogenization approaches in the best-estimate steady-state model.......... 40
Figure 16. Results for the solid temperature profiles for different thermal conductivity homogenization approaches in the best-estimate model. 41
Figure 17. Measured power in heater banks 104 and 110 during the PG-26 transient. Note that the vertical line in the power of bank 110 at 150,000 is an artefact. [2].......... 42
Figure 18. Evolution of the average temperature at the outlet of the lower reflector of the HTTF for the transient leading to the DCC in PG-26. 43
Figure 19. Results for the averaged solid temperature evolution for different thermal conductivity homogenization approaches in PG-26. 44

TABLES

Table 1. Test 1: verification of the pressure drop model in isothermal conditions. 14
Table 2. Test 2: verification of enthalpy balances in the porous media formulation. 16
Table 3. Test 3: grid convergence study for the fluid flow model in a typical hexagonal assembly of HTTF. Symbol names: IC (incompressible flow model), WC (weakly-compressible flow model). 20
Table 4. Test 4: grid convergence study for heat conduction problem in a typical HTTF hexagonal assembly. Symbol names: CC (constant thermal conductivity), TC (constant tensor conductivity), TC-VT (tensor conductivity with variable thermophysical properties).. 23
Table 5. Results for test 5. Verification of solid-liquid heat exchange coefficients for an isothermal solid problem. 25
Table 6. Test 6: grid convergence study for coupled fluid flow and solid heat conduction problem in a typical HTTF hexagonal assembly. 29
Table 7. Details of each of the homogenized assemblies for core blocks of the HTTF. 33
Table 8. Relative error in the averaged solid temperatures in the regions of interest of the HTTF at the end of the heating of PG-26, previous to the DCC transient. 45

ACRONYMS

FEM	finite-element method
FVM	finite volume method
HTR	High Temperature Reactor
MOOSE	Multiphysics Object-Oriented Simulation Environment
PDE	partial differential equation
PETSc	Portable, Extensible Toolkit for Scientific Computation

Page intentionally left blank

1. Introduction

The High Temperature Test Facility (HTTF) at Oregon State University (OSU) is an integral effects experiment designed to investigate transient behavior in high-temperature gas-cooled nuclear reactors. It is a one-quarter length-scale model of the General Atomics' Modular High Temperature Gas-cooled Reactor (MHTGR) concept design. The facility uses helium as the nominal coolant, although other gases can also be utilized. The ceramic core is heated with electrical heaters that have a maximum power of 600 kW. The HTTF is configured to simulate various postulated accidents and normal operational events in the MHTGR. Although operated at prototypical temperatures, the HTTF operates at a reduced pressure when compared to a High Temperature Reactor (HTR). The facility is primarily built to generate data for code and model validation, and does not precisely replicate MHTGR conditions, such as temperature and pressure distributions. Nevertheless, it encompasses the main physics and phenomena, associated with MHTGR transients.

The HTTF is comprised of several major components, including the reactor pressure vessel (RPV), steam generator, Reactor Cavity Simulation Tank (RCST), and Reactor Cavity Cooling System (RCCS). The primary loop consists of the reactor vessel, the heated ceramic core, steam generator, gas circulator, and connecting pipes. The RCST simulates the environment outside the MHTGR following a loss-of-flow accident. To establish boundary conditions and control radiation heat transfer from the RPV wall, the RCCS incorporates water-cooled panels surrounding the RPV. The model developed in this work involves the internal components of the reactor pressure vessel including the ceramic core, top plenum, Helium gas bypass, core barrel and cooling channels. Best-estimate boundary conditions are applied based on simulations previously performed with system codes [2].

The geometry of the HTTF is shown in Figure 1. The core of the HTTF is composed of Greencast 94-F ceramic blocks, similar to the MHTGR core configuration. It consists of a central reflector, heated core, and side reflector. Silicon carbide serves as a permanent reflector surrounding the ceramic blocks. Axially, the blocks are stacked upon one another to replicate the lower reflector, core, and upper reflector. The ceramic blocks contain 516 coolant channels (depicted in yellow) through which the helium coolant flows to remove heat. Additionally, the central reflector and side reflector contain 6 and 36 coolant channels respectively (yellow circles), mimicking bypass flow in a prototypical reactor. Graphite heater rods (depicted in red) are used for electrical heating within the core, with 210 heater rods arranged in 10 heater banks, each comprising 3 heater legs. The heated rods transmit heat by thermal radiation to the ceramic blocks. However, in this work, the rods are represented in a homogenized porous medium and heat is considered to be directly deposited in the ceramic blocks.

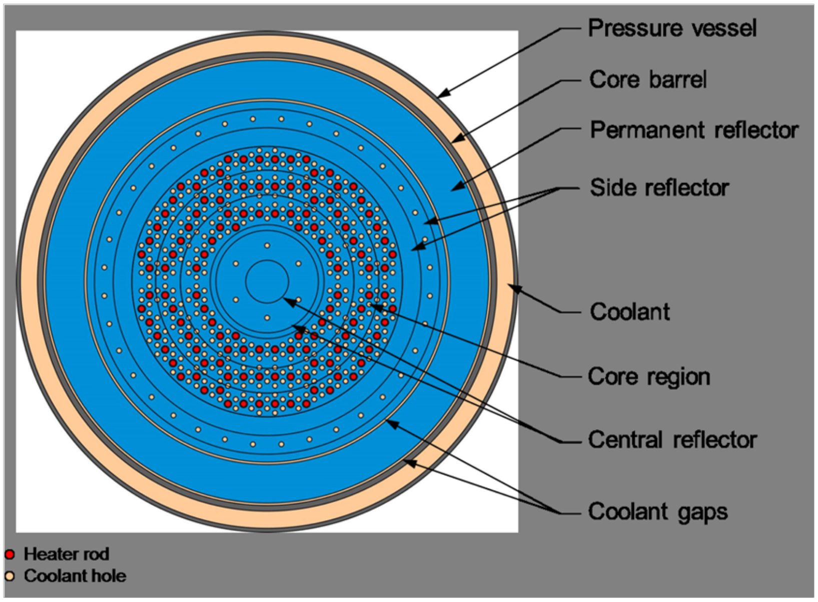

(a) Cross section of structures inside the reactor pressure vessel.

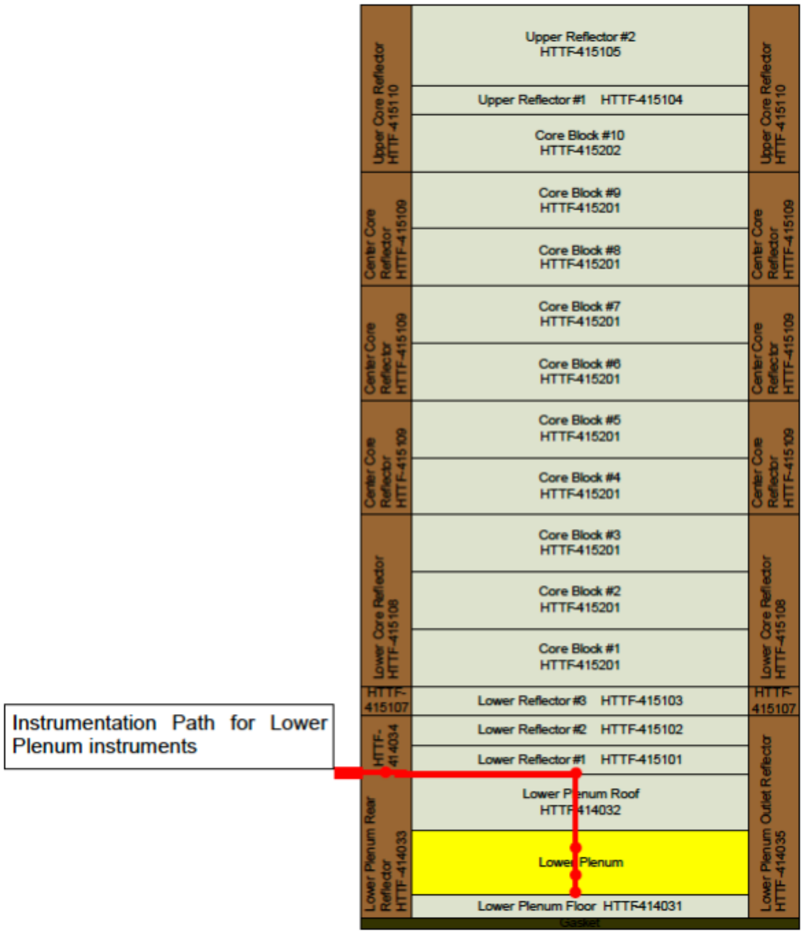

(b) Axial distribution of structures inside the reactor pressure vessel.

Figure 1: HTTF geometry.

The HTTF is equipped with a comprehensive data acquisition system, encompassing over 400 channels for thermocouples, pressure transducers, and gas sensors, strategically placed in the primary, secondary, and tertiary sectors. These instruments facilitate the measurement and monitoring of various parameters during experiments. However, the flow rate entering the HTTF core has not been measured.

In this report, we develop a Pronghorn model for the best-estimate steady state conditions of the nominal operation of the HTTF and the heating transient prior to the DCC in the PG-26 test. The initial conditions of the core before the DCC initiation were achieved by operating two out of the ten available heaters at low power (< 100 kW). The transient decay power during the DCC was scaled to match the MHTGR. The heaters were active for the first 59 hours of the test. The DCC transient was initiated during the 50th hour, involving the opening of break valves and the mixing of hot helium from the core with cold helium from the reactor cavity simulation tank (RCST). The PG-26 test was conducted from May 30, 2019, to June 30, 2019.

The report is organized as follows: Section 2 summarizes the codes used in this work. Then, in Section 4, six verification cases are presented that support the accuracy of the modeling approximations of the HTTF models in Pronghorn. Finally, in Section 5, the Pronghorn models for the HTFF facility are presented and the simulation results are compared against experimental measurements.

2. Codes and Code Jargon

The focus of this work is the development of a prismatic HTR fluid simulation capability within the Nuclear Energy Advanced Modeling and Simulation engineering-scale toolkit. The four codes used are:

- The Multiphysics Object-Oriented Simulation Environment (MOOSE) [3] is an open-source framework for discretizing partial differential equations (PDEs) using the finite-element method (FEM) and finite volume method (FVM) methods. MOOSE provides a plug-in infrastructure for various FEM and FVM simulation components, such as kernels (PDEterms), boundary conditions (PDEterms on boundaries), timestepping algorithms, general purpose objects (*UserObjects*) that the user can customize to do any desired task, etc. MOOSE is extensible by the community, encouraging contributions to the code base but allowing developers to build their own applications without contributing the code back to MOOSE; in fact, the MOOSE design allows researchers to harness all the objects in the framework in derived or MOOSE-based applications, which are commonly named after animals. In addition, MOOSE defines a custom syntax that allows a composition of complex multiphysics problems within the input file. MOOSE supports hybrid parallelism (*mpi* and threading) and scales well into the range of thousands of processors without exposing the complexity of the parallel communication to the average code contributor.
- Pronghorn [4] is a MOOSE-based, coarse-mesh thermal-hydraulics code that solves porous-medium fluid mechanics, heat transfer, and heat conduction equations for problems where the complicated geometry and interaction between fluid and solid is treated in an average sense via appropriate correlations. Pronghorn is capable of modeling steady-state and transient conditions in gas and salt-cooled pebble-bed reactors and molten-salt reactors. This work extends Pronghorn capabilities to prismatic fuel HTRs.

In addition, the following jargon is used throughout the report:

- Nonlinear variable: a variable that MOOSE solves for via the standard Portable, Extensible Toolkit for Scientific Computation (PETSc) interface provided in MOOSE. Nonlinear variables reside in the nonlinear system and are only set by MOOSE's internal solution machinery. They can be of different types, including linear continuous (*linear Lagrange*) and constant discontinuous variables (*constant monomial*).

- Auxiliary variable: all variables that are not nonlinear variables. They offer great flexibility and can be set by auxiliary kernels, transfers, or initial conditions.
- Multi-app: a system [5] that allows a MOOSE app (the *primary app*) to create additional independent MOOSE apps (the *secondary apps*) executed at user-defined points during the primary app's execution. Multi-apps can be used to create loose or Picard-type coupled equation systems. Multi-apps are flexible in the sense that a secondary app can have its own ”tertiary” apps. In this way, researchers can create arbitrary trees of MOOSE apps.
- Multi-app transfer: objects that transfer information between different apps in the multi-app tree.
- Fully coupled: all variables are solved in a single system of nonlinear equations using either Newton's or a quasi-Newton method.
- Strongly coupled: equations are split into at least two groups and solved sequentially while passing information between each other after each solution step. The term strongly coupled is usually used interchangeably with Picard iterations. However, the implication of strongly coupled equations in MOOSE jargon is that the multi-app system is used for setting up the system of equations. It is possible to use quasi-Newton methods in strongly coupled problems, and therefore, it is not strictly identical to Picard-type coupling.
- Verification: confirming that the code correctly solves equations; verification includes comparison to analytical results or the method of manufactured solutions.
- Numerical benchmarking: essentially a code-to-code comparison of results for well defined numerical benchmarks that can be performed between codes of identical fidelity levels (subchannel compared with other subchannel codes) or between different fidelity levels (subchannel compared to direct numerical simulation results).

- Validation: confirming that the code correctly solves the problem, which requires a comparison to experimental data to ensure the set of equations, assumptions, and correlations describe the physical problem of interest well. The validation for multiphysics problems against to the HTTF facility for the initial heating conditions of PG-26 is performed.

3. Theory

3.1 Porous Media Approach to prismatic fuel HTR

The flow within the fuel and control rod elements of prismatic-fuel HTRs can be modeled using a porous media model. In a porous media model, the gas and solid reflector or fuel occupy the same space. The fluid volume fraction is referred to as the porosity of the shared volume. In mathematical terms, the porosity of an assembly can be defined as follows:

$$\gamma = \frac{V_f}{V_T}, \tag{1}$$

where V_f is the flow volume and V_T is the total volume. Note that since prismatic assemblies are homogeneous in the axial direction, i.e., the geometry cross section is independent of the height in the assembly, we have $\gamma = \frac{A_f}{A_T}$ with A_f being the area of the fluid flow and A_T the total area of the assembly.

Balance equations for fluid mass, momentum, energy, and solid energy are coupled via momentum and energy exchanges described by correlations. One advantage of this approach is the ability to seamlessly couple porous flow regions to free-flow regions outside of the immediate core regions without changing the modeling paradigm. The porous flow equations for weakly-compressible flow are given by:

$$\begin{aligned}
\frac{\partial \gamma \rho}{\partial t} + \nabla \cdot (\rho \vec{v}) &= 0 \quad \text{on } \Omega_f \\
\frac{\partial \rho \vec{v}}{\partial t} + \nabla \cdot \left(\gamma^{-1} \rho \vec{v} \otimes \vec{v}\right) &= -\gamma \nabla p + \gamma \rho \vec{g} - W \rho \vec{v}_I \quad \text{on } \Omega_f \\
\frac{\partial \gamma \rho e}{\partial t} + \nabla \cdot (\rho H \vec{v}) - \nabla \cdot \left(\kappa_f \nabla T\right) + \alpha (T - T_s) &= 0 \quad \text{on } \Omega_f \\
(1-\gamma) \rho_s c_{p,s} \frac{\partial T_s}{\partial t} - \nabla \cdot (\kappa_s \nabla T_s) - \alpha (T - T_s) &= \dot{q}''' \quad \text{on } \Omega_s,
\end{aligned} \tag{2}$$

where $\vec{v}$ is the superficial velocity defined as $\vec{v} = \gamma \vec{v}_I$, with γ as the porosity and $\vec{v}_I$ as the interstitial or physical velocity, ρ is the density, p is the pressure, e is the internal energy, H is the enthalpy, T is the fluid temperature, T_s is the solid temperature, ρ_s is the solid density, $c_{p,s}$ is the specific heat of the solid phase, $\vec{g}$ is the gravity vector, W is the pressure drop coefficient, κ_f is the effective thermal conductivity of the fluid, α is the volumetric heat transfer coefficient between the fluid and the solid phase, κ_s is the effective solid thermal conductivity, and $\dot{q}'''$ is the heat source in the solid (e.g., fission heat source). For an assembly modeled as a porous medium, the fission source is defined as the total power of the assembly divided by its total volume. The effective thermal conductivities κ_f and κ_s are in general diagonal tensors.

The fluid domain Ω_f comprises porous regions with $0 < \gamma < 1$ and free flow regions with $\gamma = 1$; in the free-flow region, T_s is not solved, $\alpha = 0$, $W = 0$, and $\kappa_f = k_f$ (where k_f is the thermal conductivity of the fluid). Similarly, T_f is not solved in solid only regions where $\gamma = 0$ and $\kappa_s = k_s$ with k_s as the solid conductivity.

Eq. 2 is supplemented by the following boundary conditions:

- The flow variables p and $\vec{v}$ use specified velocity inlet, specified pressure outlet, and slip wall boundary conditions.
- The fluid energy equation has fixed temperature inflow conditions and adiabatic walls at the exterior part of the domain.
- Robin boundary conditions are applied on the boundaries between Ω_f and Ω_s:

  $$-k_s \vec{n} \nabla T_s|_{\Omega_s} - h \left(T_s|_{\Omega_s} - T|_{\Omega_f} \right) = 0, \tag{3}$$

  where h is the areal heat transfer coefficient between fluid and solid-only domains.

The following correlations are used to compute W, κ_f, κ_s, κ_f, and α.

- For all correlations, the Reynolds number is defined as:

  $$Re = \frac{D_h \rho \|\vec{u}_I\|}{\mu}, \tag{4}$$

  where D_h is the hydraulic diameter of the fuel element.
- The Churchill drag coefficient [6] is used to compute the drag coefficient in all assembly

regions and is a diagonal tensor given by:

$$W = \begin{bmatrix} 100w & 0 & 0 \\ 0 & 100w & 0 \\ 0 & 0 & w \end{bmatrix}, \tag{5}$$

where we assume the flow channels are are aligned with the z-direction and the modification of the drag coefficients in the x-y plane is so that negligible nonphysical cross flows appears in the transverse direction. The value of w is computed by:

$$w = \gamma f \frac{\|\vec{v}_I\|}{2D_h}, \tag{6}$$

f is defined by the Churchill friction factor as follows:

$$f = 8\left[\left(\frac{8}{Re}\right)^{12} + \frac{1}{(\theta_1+\theta_2)^{1.5}}\right]^{\frac{1}{12}}, \tag{7}$$

with the following definitions for θ_1 and θ_2:

$$\theta_1 = \left[-2.457\ln\left(\left(\frac{7}{Re}\right)^{0.9} + 0.27\tilde{\epsilon}\right)\right]^{16}, \tag{8}$$

$$\theta_2 = \left(\frac{37530}{Re}\right)^{16}, \tag{9}$$

where $\tilde{\epsilon}$ is the relative rugosity of the channels.

- For the HTTF there are no cross flows for the coolant channels and the fluid flows only in the axial direction; hence, the effective thermal conductivity tensor for the fluid κ_f is expressed as follows:

$$\kappa_f = \begin{bmatrix} 0 & 0 & 0 \\ 0 & 0 & 0 \\ 0 & 0 & \gamma k_f \end{bmatrix} \tag{10}$$

- The effective thermal conductivity tensor of the solid matrix κ_s is different in the transversal and axial directions and is expressed as follows [7]:

$$\kappa_s = \begin{bmatrix} (1-\gamma)\kappa_{s,t} & 0 & 0 \\ 0 & (1-\gamma)\kappa_{s,t} & 0 \\ 0 & 0 & (1-\gamma)k_s \end{bmatrix}, \tag{11}$$

where k_s is the thermal conductivity of the solid and $\kappa_{s,t}$ is the effective thermal conductivity of the solid in the transverse direction. Three different bounding approaches are compared for this conductivity:

$$\kappa_{s,t} = \gamma k_f + (1-\gamma)k_s\,, \tag{12}$$

$$\kappa_{s,t} = \left(\frac{\gamma}{k_f} + \frac{1-\gamma}{k_s}\right)^{-1}. \tag{13}$$

and

$$\kappa_{s,t} = (\gamma k_f)^{\alpha_f}((1-\gamma)k_s)^{\alpha_s}\,. \tag{14}$$

In this work, we will generically take $\alpha_f = \alpha_s = 0.5$, which constitutes the standard root mean squared average of the thermal conductivity. However, in practice specific methods must be developed for fitting these exponents to the conditions of the homogenized cells.

- The volumetric heat transfer coefficient α is computed using the approach in Reference [8], which, for the simple flow in the axial direction only reduces to:

  $$\alpha = \frac{A_f}{V_T}h, \tag{15}$$

  where A_f is the surface area of the flow channels within an assembly and h is computed via the Dittus-Boelter correlation [9]:

  $$h = \frac{k_f}{D_h}0.023Re^{0.8}Pr^{0.4}, \tag{16}$$

  where Pr is the Prandtl number.

4. Verification of porous media implementation

The distance between code/simulation prediction and physical reality is affected by two sources of error. First, the error inherent in the mathematical models to represent the physical world. Second, the error in the numerical implementation of said mathematical model. In this context, verification is a crucial part for high-temperature reactor (HTR) modeling, to ensure that the numerical schemes implementing the mathematical models are accurate and reliable. Salient reasons why verification is important for HTRs are:

1. **Accuracy and Credibility**: Verification ensures that the code's numerical implementation of the mathematical models used to simulate HTR behavior is accurate and reliable. By comparing the code predictions against known analytical solutions and performing mesh convergence studies, the accuracy and credibility of the numerical schemes can be established.

2. **Model Development and Improvement**: Verification informs the development and improvement of HTRs models. By comparing code predictions with reference solutions, discrepancies and errors can be identified, leading to the refinement and enhancement of the modeling approach. Simple verification exercises provide valuable feedback to model developers, allowing them to identify and rectify any deficiencies or limitations in the model formulation, assumptions, and to guide development of more elaborate models.

3. **Sensitivity and Uncertainty Analysis**: Verification is essential for conducting sensitivity and uncertainty analysis, which is not performed in this work but may be performed in future iterations of this modeling effort. Once the accuracy of the models has been established through verification, the code can be used to assess the sensitivity of the HTRs behavior to various input parameters or uncertainties. Sensitivity and uncertainty analysis provide insights into the robustness and reliability of the code predictions, helping to identify key parameters and sources of uncertainty that may significantly affect the results.

4. **Regulatory Compliance**: Pronghorn verification for HTRs is required for regulatory compliance if the code is used for seeking approval or licensing for HTRs designs. United

States Nuclear Regulatory Commission requires evidence that the models used for safety analyses and assessments are verified against established standards and benchmark problems. This verification is a first step to ensuring that the modeling approach meets the required standards, providing confidence to regulatory bodies and stakeholders in the safety and reliability of the HTRs design.

In summary, verification plays a critical role in HTRs thermal-hydraulics modeling by ensuring the accuracy, credibility, and reliability of the mathematical models and computational implementation of Pronghorn. Validation is meaningless without first verifying the numerical implementation. Verification allows for the development, improvement, and validation of the models, enhances their predictive capabilities, and provides confidence in the results obtained from HTRs simulations. These are the reasons why a comprehensive verification work is developed in this section.

4.1 Test 1: Verification of Friction Factors in Steady-State, Isothermal Conditions

The verification problem consists of a pipe that emulates a representative cooling channel of the HTTF. The flow is modeled as an incompressible flow. The following thermophysical properties and boundary conditions are assumed for the flow in the pipe simulating the conditions expected for the HTTF:

- Density: $\rho = 1.0 \frac{\text{kg}}{\text{m}^3}$
- Dynamic Viscosity: $\mu = 10^5 \text{Pa.s}$
- Inlet Velocity: $10 \frac{\text{m}}{\text{s}}$

The pipe diameter $D \in [10^{-3}, 1]$m is varied to change the Reynolds number. The pressure drop predicted by the friction correlation using Darcy friction factors Eq. 17 as implemented in Pronghorn, is compared against analytical pressure drop calculations using the Fanning friction factor as predicted by the Churchill [6] and the Haaland [10] correlations. These equations read as follows:

Churchill Correlation for Fanning Friction Factor:

$$f = 2\left[\left(\frac{8}{Re}\right)^{12} + \frac{1}{(\theta_1+\theta_2)^{1.5}}\right]^{\frac{1}{12}} , \tag{17}$$

with the following definitions for θ_1 and θ_2:

$$\theta_1 = \left[-2.457\ln\left(\left(\frac{7}{Re}\right)^{0.9} + 0.27\tilde{\epsilon}\right)\right]^{16} , \tag{18}$$

$$\theta_2 = \left(\frac{37530}{Re}\right)^{16} . \tag{19}$$

Haaland Correlation for Fanning Friction Factor:

$$\frac{1}{\sqrt{f}} = -2\log\left(\frac{\epsilon/D}{3.7} + \frac{2.51}{Re\cdot\sqrt{f}}\right) \tag{20}$$

The results are presented in Table 1. For all tests, an axially converged mesh is used. The Pronghorn results match hand-calculations using the Churchill friction factor exactly and consequently the error is zero for all Reynolds numbers. The difference of Pronghorn compared with hand-calculations using Haaland's correlation is between 0.2 and 4%. This comparison shows that the choice of the correlation can affect the solution significantly. As we match hand calculations exactly, we qualify this verification test with a **PASS** status.

Table 1: Test 1: verification of the pressure drop model in isothermal conditions.

Dh [m]	1	0.5	0.1	0.01	0.001
Re	1.00×10^6	5.00×10^5	1.00×10^5	1.00×10^4	1.00×10^3
$\Delta p_{\text{Churchill}}$ [Pa]	1.15×10^0	2.59×10^0	1.77×10^1	3.07×10^2	6.34×10^3
Δp_{MOOSE} [Pa]	1.15×10^0	2.59×10^0	1.77×10^1	3.07×10^2	6.34×10^3
Δp_{Moody} [Pa]	1.15×10^0	2.59×10^0	1.77×10^1	3.06×10^2	6.54×10^3
Error Pronghorn vs. Churchill	0%	0%	0%	0%	0%
Error Pronghorn vs. Haaland	0.22%	0.24%	0.29%	0.39%	−3.24%

4.2 Test 2: Verification of Enthalpy Balance

Here we examine a characteristic assembly of the HTTF facility. The geometry and discretization used for this assembly is depicted in Figure 2. The mesh discretization has been converged axially so that the results are mesh-independent. The thermal flow is assumed to be incompressible and the following thermophysical properties and boundary conditions are assumed:

- Density: $\rho = 1.0 \frac{\text{kg}}{\text{m}^3}$
- Dynamic Viscosity: $\mu = 10^5 \text{Pa.s}$
- Inlet Velocity: $1 \frac{\text{m}}{\text{s}}$
- Specific Heat at Constant Pressure: $C_p = 1000 \frac{\text{J}}{\text{kg.K}}$
- Volumetric Heat Source: $q''' = 10^6 \frac{\text{W}}{\text{m}^3}$

The walls of the geometry are assumed adiabatic. The flow direction is from top to bottom and the fluid is heated as it progresses from the inlet to the outlet. As observed in Figure 2 there is no radial heat conduction, due to the symmetry of the problem. Assuming these conditions, one can compute the analytical solution for the temperature rise across the assembly. This solution reads as follows:

$$\Delta T = \frac{q''' L}{\rho_f c_{p,f} u_s} \,. \tag{21}$$

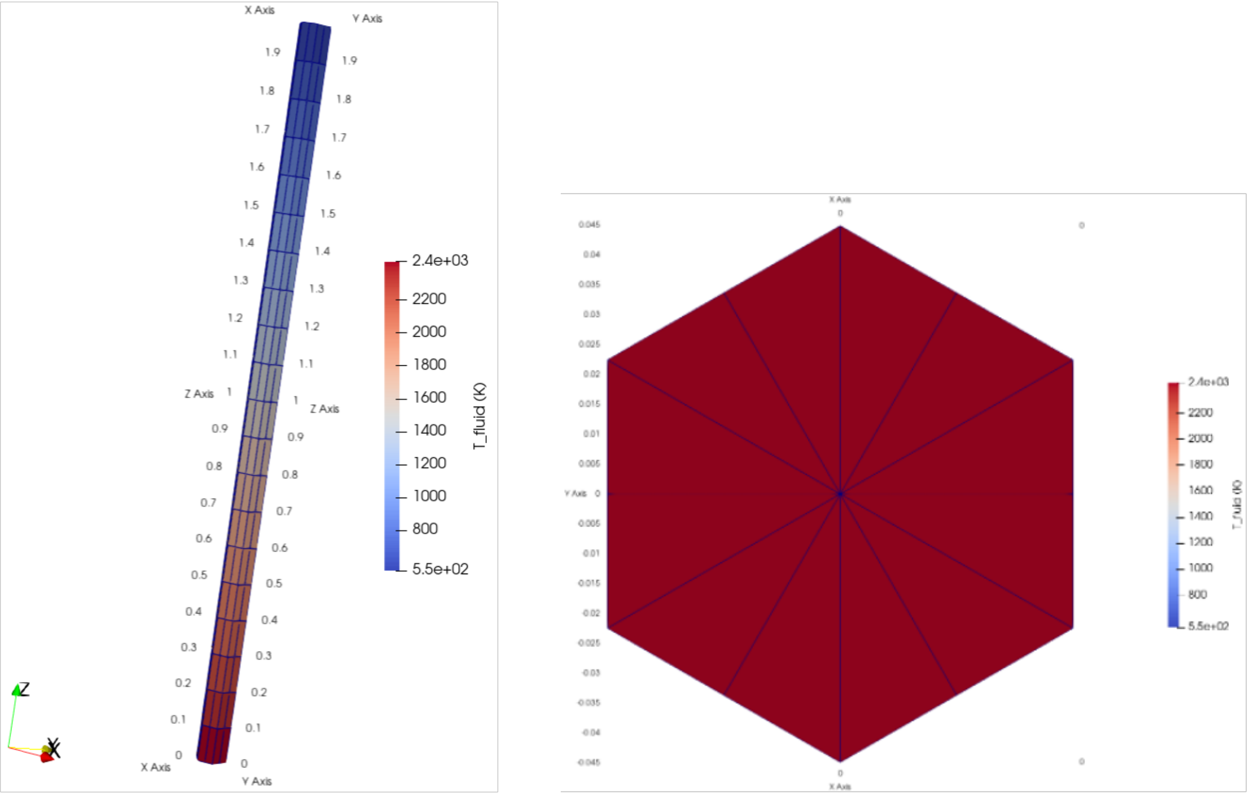

(a) Axial temperature profile.

(b) Radial temperature profile.

Figure 2: Geometry, temperature profiles, and computational mesh for Test 2.

In this case, the temperature rise depends only on the superficial velocity and not on the porosity. Hence, the solution obtained should be independent of porosity. To verify this, Pronghorn simulations are performed with varying porosity and hence, varying Reynolds number due to the varying interstitial velocity. The obtained results are presented in Table 2. As observed from the table, the numerical solution is in good agreement with the analytical solution with the residual discrepancy attributed to iterative convergence error. We qualify this verification test with a **PASS** status.

Table 2: Test 2: verification of enthalpy balances in the porous media formulation.

Re	1.00×10^3	1.25×10^3	1.67×10^3	2.50×10^3	5.00×10^3
Porosity	1	0.8	0.6	0.4	0.2
ΔT	1.98×10^3	1.98×10^3	1.98×10^3	1.98×10^3	1.98×10^3
ΔT_{MOOSE}	1.98×10^3	1.98×10^3	1.98×10^3	1.98×10^3	1.98×10^3
Error	-5.07×10^{-4}	-4.05×10^{-4}	-3.04×10^{-4}	-2.02×10^{-4}	-1.01×10^{-4}

4.3 Test 3: Grid Convergence Analyses for Fluid Flow

For the next verification test, the mesh convergence for the thermal fluid flow is analyzed in the typical HTTF assembly shown in Figure 2. Grid convergence analysis is an essential technique in computational fluid dynamics (CFD), including thermal fluid flow simulations. It aims to assess the accuracy and reliability of numerical solutions obtained from different grid resolutions and determine the monotonic convergence of the associated numerical system. In this verification exercise of coarse-mesh CFD, grid convergence is used to ensure that under grid refinement the solution converges.

The main purposes of performing a grid convergence study are the following:

1. Verification of numerical methods: Grid convergence analysis helps verify the numerical methods used in Pronghorn simulations. By comparing solutions obtained on different grids, we evaluate the convergence behavior and consistency of the numerical scheme. It helps ensure that the simulation results are not strongly dependent on the grid resolution and that the numerical errors are sufficiently small. This aspect ultimately helps to determine an adequate axial mesh discretization for the full core HTTF simulations.

2. Quantifying discretization errors: Discretization errors arise from approximating the continuous governing equations of fluid flow with discrete equations on a computational grid. Grid convergence analysis provides a quantitative measure of these errors and the order of accuracy by examining the solution convergence as the grid is refined. It helps identify regions of the flow field where the numerical solution may deviate significantly from the true solution due to inadequate grid resolution. In this analysis, these errors are quantified up to convergence tolerance.

3. Optimal grid selection: Grid convergence analysis helps determine the optimal grid resolution for a given simulation. It involves performing simulations on successively refined grids until the solution converges to a desired level of accuracy. This analysis guides the selection of an appropriate grid resolution, balancing computational cost and accuracy requirements. It ensures that the chosen grid is fine enough to capture the relevant flow features and thermodynamic phenomena accurately, while maintaining a reasonable

computational cost.

4. Quality assurance: Grid convergence analysis is an important step in quality assurance for Pronghorn simulations. It helps establish the credibility and robustness of the numerical models and simulations by demonstrating that the results are grid-independent within acceptable error limits. It is a fundamental practice in scientific and engineering research to ensure that the simulations are accurate and reliable.

In summary, grid convergence analysis is performed for thermal fluid flow simulations to verify numerical methods, quantify discretization errors, select optimal grid resolutions, estimate errors, and ensure the quality and reliability of the simulation results.

For the fluid flow properties, Pronghorn's database of helium fluid properties is utilized. As these properties are dependent on pressure and temperature, this approach requires us to set the outlet pressure condition in the fuel assembly as a boundary condition. The following internal and boundary conditions are used for this test:

- Inlet Velocity: $2\frac{\mathrm{m}}{\mathrm{s}}$
- Inlet Temperature: 380K
- Outlet Pressure: 200×10^3Pa
- Hydraulic Diameter: 10^{-2}m
- Volumetric Heat Source: $q''' = 10^6\frac{\mathrm{W}}{\mathrm{m}^3}$
- Porosity: 0.5

The radial discretization of the fuel assembly is shown in Figure 2. The axial discretization is always uniform and the number of axial levels is varied. We denote N_a the number of axial levels and the resulting height of the axial cells is $\Delta z = \frac{L}{N_a}$, where $L = 1.981$m is the axial length of the fuel assembly.

The Grid Convergence Analysis (GCI) in the axial direction is performed following the Richardson extrapolation formalism. The order of convergence p for a given observable quantity

f is first estimated as follows:

$$p = \frac{\ln\left(\frac{f_3 - f_2}{f_2 - f_1}\right)}{\ln(r)}\,, \tag{22}$$

where f_i is the observable quantity for refinement level i and r is the refinement ratio between these levels. We will use two observable quantities in this analysis, the axial pressure drop (ΔP) and the total temperature rise (ΔT) across the assembly. The computed convergence index for the Pronghorn simulation for each of these observable quantities are:

$$p_{\Delta P} = 1.52\,, \tag{23}$$

$$p_{\Delta T} = 1.00\,, \tag{24}$$

where the first order of convergence for temperature comes from the first order upwind discretization used for advection in the energy conservation equation.

With the order of convergence computed for each observable quantity, the GCI is computed as follows:

$$GCI = \frac{|\epsilon|}{r^p - 1}\,, \tag{25}$$

$$\epsilon = \frac{f_2 - f_1}{f_1}\,. \tag{26}$$

Two formulations are considered for the fluid flow, namely incompressible and weakly-compressible. Note that since neither formulation includes the pressure-dependent compressibility effects in the gas, the same steady-state solutions are expected for both formulations. This serves as a further verification of both formulations.

The results obtained for the pressure drop and temperature rise for both formulations is presented in Table 3. Additionally, the GCI analyses for each observable quantity and formulation are also presented. The convergence tolerance for the relative residuals is set to 10^{-3} as a reasonable engineering convergence criterion for thermal-hydraulics simulations. As observed in the table, using 16 axial levels for the axial discretization (i.e., $\Delta z = 0.124$m) already provides a GCI $\sim$ 1%, which is less than the errors expected in the approximations introduced in the thermal-hydraulics modeling.

Table 3: Test 3: grid convergence study for the fluid flow model in a typical hexagonal assembly of HTTF. Symbol names: IC (incompressible flow model), WC (weakly-compressible flow model).

		Axial Levels					
Observable	Model	4	8	16	32	64	128
ΔP [Pa]	IC	2.23E+02	2.15E+02	2.12E+02	2.10E+02	2.10E+02	2.10E+02
	WC	2.23E+02	2.15E+02	2.12E+02	2.10E+02	2.10E+02	2.10E+02
ΔT [K]	IC	8.46E+02	7.99E+02	7.76E+02	7.64E+02	7.64E+02	7.64E+02
	WC	8.46E+02	7.99E+02	7.76E+02	7.64E+02	7.64E+02	7.64E+02
GCI ΔP [Pa]	IC	5.92E-02	2.15E-02	8.44E-03	0.00E+00	0.00E+00	-
	WC	5.92E-02	2.15E-02	8.44E-03	0.00E+00	0.00E+00	-
GCI ΔT [K]	IC	8.57E-02	4.54E-02	2.34E-02	0.00E+00	0.00E+00	-
	WC	8.57E-02	4.54E-02	2.34E-02	0.00E+00	0.00E+00	-

Since the solver shows monotonic convergence and the GCI converges under successive refinements, we qualify this verification test with a **PASS** status.

4.4 Test 4: Grid Convergence Analyses for the Thermal Conduction Problem.

As further verification exercise a heat conduction problem with internal heat source is solved. This problem has two additional complexities in comparison to a standard heat conduction problem:

1. As shown in Eq. 11, the solid conductivity is not isotropic but has a tensor form. For this verification test, the radial solid conductivity homogenization follows the volume-average approach.
2. The thermal reflector's thermophysical properties, which are built out of G-348 material, have a strong dependence on temperature.

The material used to build the solid blocks of the HTTF facility was Greencast 94-F. Greencast 94 is mainly composed of 94% Alumina (Al_2O_3), 5% Lime (CaO), and a few trace elements. The thermophysical properties of Greencast 94-F have been reported in OSU's HTTF Design Documentation [1]. In this work, we used the table reported properties to fit polynomials for each material property, which can be easily introduced to Pronghorn via the *SolidProperties* module. The fitted data for density, specific heat, and thermal conductivity is presented in Figure 3.

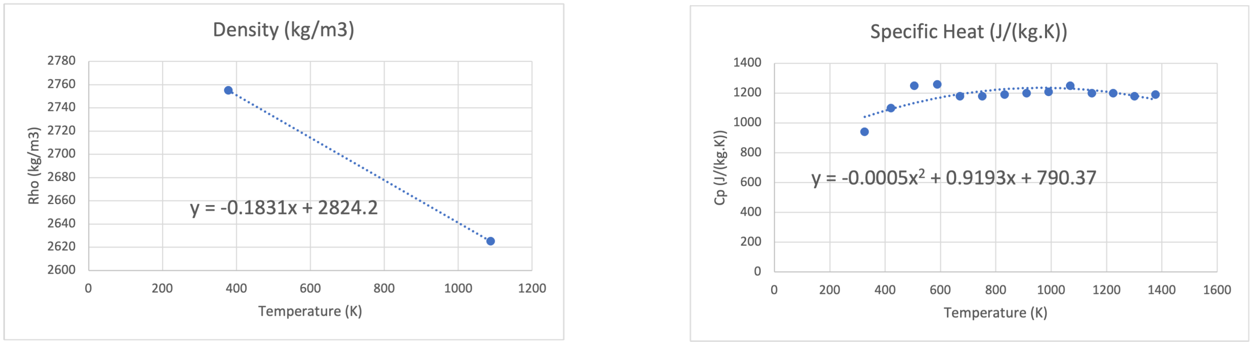

(a) Density.

(b) Specific Heat at Constant Pressure.

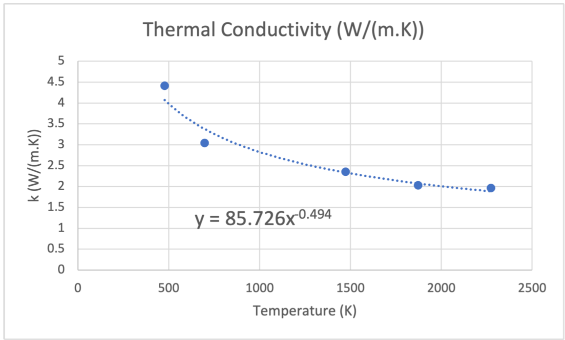

(c) Thermal Conductivity.

Figure 3: Measured thermophysical properties for Greecast 94-F [1].

The problem solved for this verification test case is a heat conduction problem within the solid block of an HTTF hexagonal fuel assembly. Note that the fuel assemblies are heated by electric resistances emulating the fuel rod heating in an actual HTR. A fixed temperature boundary condition is imposed in the top part of the assembly, emulating the temperature homogenization at the top plenum of the HTTF, and a convective heat flux boundary condition is imposed in the bottom face, which mimics the effects of lower plenum mixing. The following characteristics are assigned to the problem:

- Top Boundary Temperature: 380K
- Bottom Boundary Convection : $10 \frac{\mathrm{W}}{\mathrm{m}^2.\mathrm{K}}$
- Bottom Boundary Free Convection Temperature: 380K
- Volumetric Heat Source: $q''' = 10^4 \frac{\mathrm{W}}{\mathrm{m}^3}$
- Porosity: 0.1831

The computed temperature field is depicted in Figure 4. As expected, for the axial temperature profile, the fuel heats up towards the free convection boundary condition placed at the bottom of the assembly. There is no thermal gradient observed in the radial direction due to the symmetry of the problem. This observation is important because it implies that the constant and tensor conductivity formulations should yield the same results.

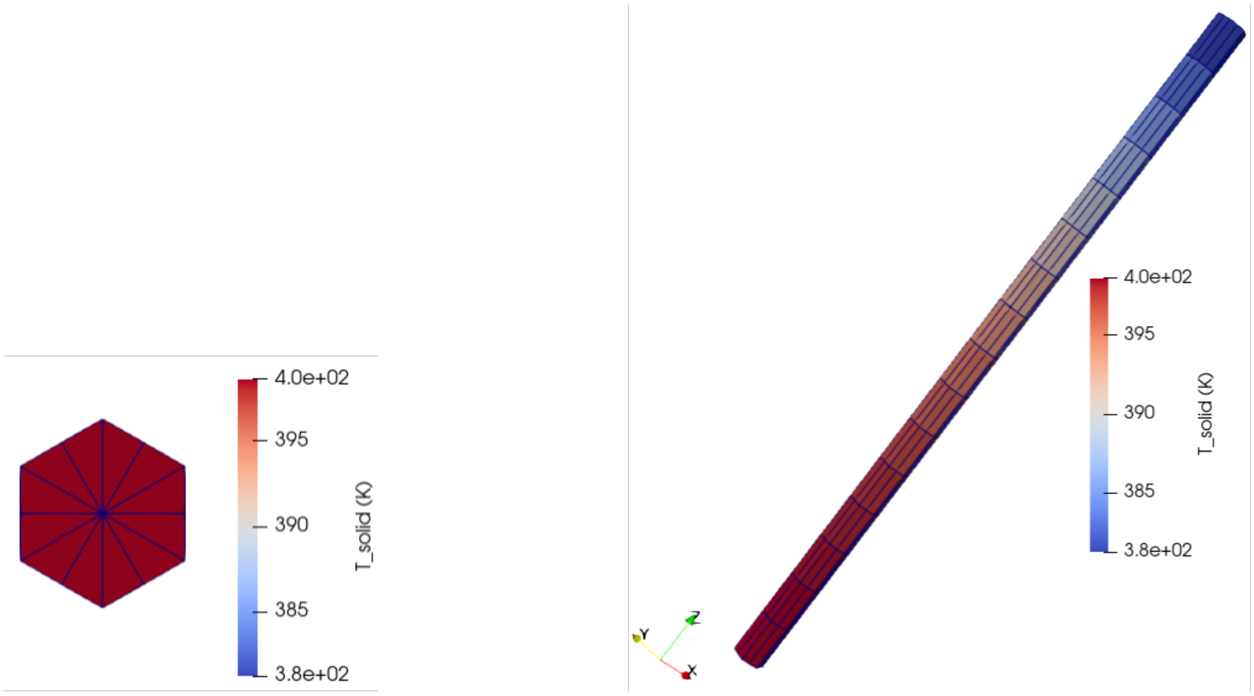

(a) Radial temperature profile.

(b) Axial temperature profile.

Figure 4: Geometry, temperature profiles, and computational mesh for Test 4.

For the grid convergence study, three simultaneous analyses are performed using:

1. a homogeneous constant conductivity (CC),
2. a tensor constant conductivity (TC),
3. a tensor conductivity with variable thermophysical properties (TC-VT).

The mesh convergence study is performed by varying the discretization in the axial direction, while keeping a constant radial discretization. The grid convergence index obtained in each case is $p = 2$, which is expected for the finite volume solution of the heat conduction problem in Pronghorn. Two observable quantities are selected, the average and the maximum temperature in the assembly.

The calculated observable quantities and the computed GCI, for successively refined meshes and for each formulation are presented in Table 4. As expected, the solutions for the constant and tensor conductivity are identical. This suffices for the verification of the implementation of the conductivity tensor. Additionally, we observe that the mesh convergence for the cases with constant thermophysical properties is faster than the ones with variable thermophysical properties. This is expected as the cases with variable thermophysical properties add the variation of the properties with temperature to the numerical system, which requires a finer grid for convergence. The convergence tolerance for the problem is set to 10^{-8}. Even though this is probably too restrictive for practical applications, we need a tighter convergence tolerance to have a feasible GCI analysis. Similar to Test 3, selecting 16 levels for the axial direction already provides a GCI of $\sim 5 \times 10^{-6}$, which is completely acceptable considering that is much smaller than the errors yielded by the modeling assumptions. We qualify this verification test with a **PASS** status.

Table 4: Test 4: grid convergence study for heat conduction problem in a typical HTTF hexagonal assembly. Symbol names: CC (constant thermal conductivity), TC (constant tensor conductivity), TC-VT (tensor conductivity with variable thermophysical properties).

		Axial Levels					
Observable	Model	4	8	16	32	64	128
Av. T [K]	CC	4.06E+02	4.05E+02	4.05E+02	4.05E+02	4.05E+02	4.05E+02
	TC	4.06E+02	4.05E+02	4.05E+02	4.05E+02	4.05E+02	4.05E+02
	TC-VT	3.93E+02	3.93E+02	3.93E+02	3.93E+02	3.93E+02	3.93E+02
Max T [K]	CC	4.16E+02	4.16E+02	4.16E+02	4.16E+02	4.16E+02	4.16E+02
	TC	4.16E+02	4.16E+02	4.16E+02	4.16E+02	4.16E+02	4.16E+02
	TC-VT	3.99E+02	3.99E+02	3.99E+02	3.99E+02	3.99E+02	3.99E+02
GCI - Av. T [K]	CC	1.85E-03	3.82E-07	0.00E+00	0.00E+00	0.00E+00	-
	TC	1.85E-03	3.82E-07	0.00E+00	0.00E+00	0.00E+00	-
	TC-VT	1.07E-03	2.69E-04	6.70E-05	1.69E-05	4.33E-06	-
GCI - Max T [K]	CC	7.12E-04	3.72E-07	0.00E+00	0.00E+00	0.00E+00	-
	TC	7.12E-04	3.72E-07	0.00E+00	0.00E+00	0.00E+00	-
	TC-VT	1.84E-04	1.66E-04	5.43E-06	8.54E-06	1.16E-06	-

4.5 Test 5: Verification of the Coupled Fluid-Solid Convection Problem.

The problem emulates a fuel assembly of the HTTF. The problem is schematically shown in Figure 5. A helium flow though a pipe is heated by a solid assembly. For simplicity, the temperature of the solid is assumed constant in this problem. The cross-sectional area of the fuel assembly is fixed, whereas its porosity depends on the diameter of the pipe embedded in the fuel assembly that is varied during the studies. The coolant in the pipe is heated up from inlet to outlet.

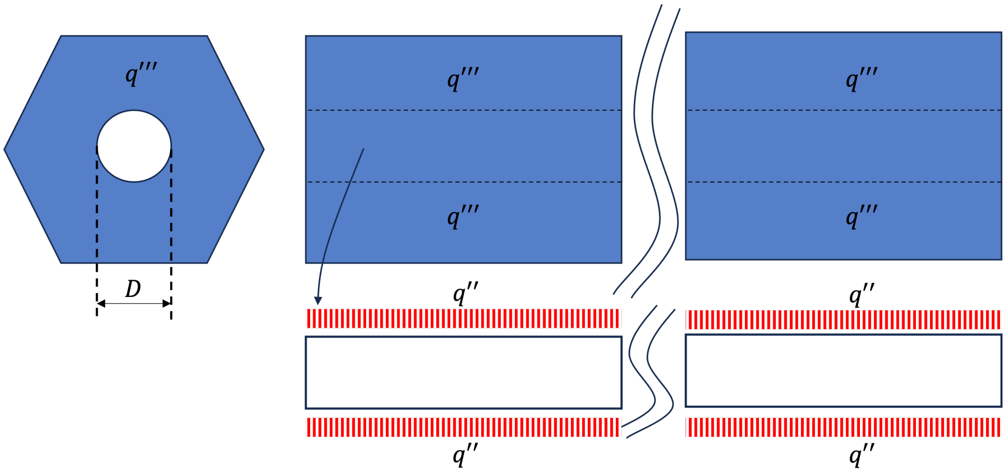

Figure 5: Geometrical representation of the modeled geometry in Test 5.

Due to the constant solid temperature, one can integrate the temperature in the pipe to find an analytical solution for the temperature as a function of the axial distance z. The solution reads as follows:

$$T(z) = T_{solid} + (T_{in} - T_{solid})e^{-\frac{4h}{\rho c_p D v}z}, \tag{27}$$

where T_{solid} is the fixed solid temperature, T_{in} is the inlet fluid temperature, h is the heat transfer coefficient (assumed to be constant over the pipe length and computed using the Dittus-Boelter correlation 16), ρ is the density, c_p is the constant specific heat at constant pressure, D is the pipe diameter, and v is the bulk speed of the flow in the pipe, which is equal to the interstitial velocity in the porous media simulation. The challenge is to match the analytical solution with the numerical solution computed by Pronghorn, in which the fluid flow is homogenized over the whole assembly.

In the problem simulation we set the superficial velocity in the assembly to $1\frac{\text{m}}{\text{s}}$ and vary the pipe diameter. Hence, the interstitial velocity in the assembly, or flow velocity in the pipe, is implicitly determined by the quotient of the superficial velocity and the porosity of the assembly. For simplicity, we assume the following constant thermophysical properties for the flow in the pipe:

- Density: $\rho = 1.0\frac{\text{kg}}{\text{m}^3}$
- Dynamic Viscosity: $\mu = 10^5\text{Pa.s}$
- Specific Heat at Constant Pressure: $C_p = 1000\frac{\text{J}}{\text{kg.K}}$
- Thermal Conductivity: $0.01\frac{\text{W}}{\text{m.K}}$

The results obtained for the Test are presented in Table 5. A very good agreement is observed in the outlet temperature between the analytical and the numerical solution. The error between them is smaller than 1%, which is acceptable considering the errors introduced by the modeling assumptions. As the pipe diameter gets smaller, the flow speed in the pipe increases and hence, a larger heat exchange coefficient is achieved leading to higher outlet temperatures. Additionally, the axial temperature profile for the analytical solution and the one predicted by Pronghorn for the test case with porosity of 0.03 (i.e., $D = 0.02m$) are compared in Figure 6. Excellent agreement is observed between the numerical and analytical solution. Therefore, we qualify this verification test with a **PASS** status.

Table 5: Results for test 5. Verification of solid-liquid heat exchange coefficients for an isothermal solid problem.

Dh [m]	2.00E-02	4.00E-02	8.00E-02	1.00E-01
Perimeter [m]	6.28E-02	1.26E-01	2.51E-01	3.14E-01
Area [m^2]	3.14E-04	1.26E-03	5.03E-03	7.85E-03
Porosity	3.00E-02	1.20E-01	4.80E-01	7.51E-01
Interstitial Vel. [m/s]	3.33E+01	8.33E+00	2.08E+00	1.33E+00
Re	6.66E+04	3.33E+04	1.67E+04	1.33E+04
Pr	1.00E+00	1.00E+00	1.00E+00	1.00E+00
Nu	1.66E+02	9.54E+01	5.48E+01	4.58E+01
h [W/(m^2.K)]	8.31E+01	2.39E+01	6.85E+00	4.58E+00
A/V [1/m]	6.01E+00	1.20E+01	2.40E+01	3.00E+01
Analytic T [K]	7.69E+02	6.49E+02	5.53E+02	5.28E+02
Computed T [K]	7.69E+02	6.48E+02	5.52E+02	5.28E+02
Error	0.05%	0.03%	0.02%	0.11%

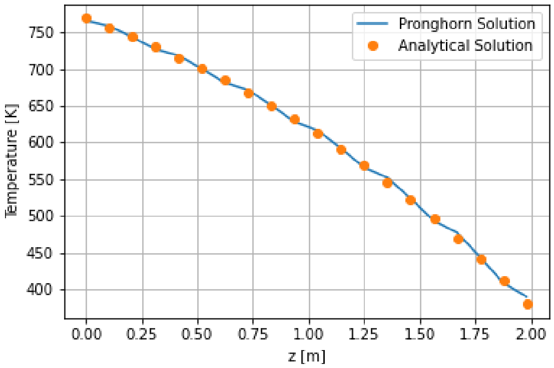

Figure 6: Test 5: verification exercise for heat exchange coefficients.

4.6 Test 6: Grid Convergence Analyses for the Conjugated Heat Transfer.

Performing a mesh convergence study for conjugate heat transfer problems in nuclear applications is important to ensure the accuracy and reliability of the simulation results. Conjugate heat transfer simulations involve the analysis of heat transfer phenomena across multiple domains with different material properties, such as solid structures and fluid regions. In nuclear applications, these simulations are crucial for studying thermal behavior, safety analysis, and optimization of nuclear system design.

Test 6 consists of the mesh convergence study for the conjugated heat transfer porous media model. A surrogate fuel element of the HTTF facility is modeled. The power source is directly applied to the solid region of the assembly and heat is transferred to the fluid by means of convection. The coolant is helium gas, while the solid block in the assembly is composed by Greencast 94-F. Thermophysical properties dependent on temperature are considered for both the solid blocks and the coolant flow. In brief, the full model described in Section 3.1 is used in this test.

The goals of the grid convergence studies performed are the following:

1. Accurate representation of thermal development length: In conjugate heat transfer problems, the thermal development length plays a significant role in capturing the heat transfer characteristics at the entry of the assembly. The mesh resolution should be fine enough to adequately resolve this thermal entry length, where temperature gradients are

large and flow pattern changes are significant.

2. Resolution of thermal gradients: HTRs often exhibit complex thermal gradients due to the presence of various components, coolant regions, and heat sources. A mesh convergence study ensures appropriate resolution of thermal gradients over the HTTF assembly. It ensures that the mesh captures the fine-scale variations in temperature accurately, enabling reliable predictions of temperature distributions.

3. Validation of heat transfer mechanisms: Conjugate heat transfer involves the interaction between solid structures and fluid flows, including convective heat transfer, conductive heat transfer, and radiative heat transfer. Only the first two are modeled in this work. Radiative heat transfer will be included in the future. The mesh convergence analysis helps to verify the accuracy of the heat transfer mechanisms modeled in the simulation. By refining the mesh and observing the convergence behavior of the results, one can assess whether the chosen mesh adequately captures the interactions between the solid and fluid domains.

In summary, a mesh convergence study is crucial for conjugate heat transfer simulations in nuclear problems to accurately resolve thermal gradients, validate heat transfer mechanisms, and quantify discretization errors. Since axial heating of the flowing helium coolant is a dominating mechanism over radial heat conduction in the HTTF core, it is sufficient to perform the grid convergence analysis for one characteristic assembly of the facility. The heated assembly is chosen as these will be the ones reaching the highest temperature gradients and hence, the largest variations of thermophysical properties. It is expected that larger variations in the thermophysical properties will cause a slower grid convergence as the numerical system's condition keeps changing under successive mesh refinements due to changing temperature and thermophysical properties at each element. Performing the mesh convergence study ensures the reliability and accuracy of the simulation results, enabling informed decision-making in the full HTTF facility model.

The following boundary and internal conditions are used for the test:

- Inlet Fluid Temperature: 380K,
- Top Solid Fixed Temperature: 380K,

- Inlet Superficial Velocity: $0.3969\frac{\mathrm{m}}{\mathrm{s}}$,
- Assembly Lateral Walls: Adiabatic for both Solid and Fluid,
- Outlet Fluid Temperature: Free Flow,
- Outlet Solid Temperature: Free Convection with Heat Exchange Coefficient $h = 10\frac{\mathrm{W}}{\mathrm{m}^2.K}$ and Free Convection Temperature $380K$,
- Outlet Pressure: $200 \times 10^3\mathrm{Pa}$,
- Hydraulic Diameter for Fluid Flow: 0.01m,
- Porosity: 0.1831,
- Power Source: $10^5\frac{\mathrm{W}}{\mathrm{m}^3}$.

The observable quantities chosen for the GCI analyses are the average temperature, maximum temperature, and pressure drop across the assembly. The following convergence indexes have been computed for each observable quantity:

$$p_{T_{av}} = 1.65\,, \tag{28}$$

$$p_{T_{max}} = 1.05\,, \tag{29}$$

$$p_{\Delta p} = 0.93 \tag{30}$$

The results obtained for the mesh convergence analysis are presented in Table 6. A monotonic convergence is obtained for all observable quantities. Note that the temperature values are slightly higher than the ones that would be obtained if the radial heat conduction was considered in this model. Furthermore, with an axial discretization of 16 cells, the GCI for the temperatures is $< 1\%$ and the one for pressure is $\sim 2\%$. These errors are smaller than the expected errors in the porous media modeling assumptions of the HTTF facility. Hence, we qualify this test with a **PASS** status.

Table 6: Test 6: grid convergence study for coupled fluid flow and solid heat conduction problem in a typical HTTF hexagonal assembly.

Axial Levels	**4**	**8**	**16**	**32**	**64**	**128**
Av. Temp. [K]	9.64E+02	9.52E+02	9.48E+02	9.47E+02	9.47E+02	9.46E+02
Max Temp. [K]	1.21E+03	1.20E+03	1.20E+03	1.20E+03	1.20E+03	1.20E+03
ΔP [Pa]	3.26E+01	3.41E+01	3.49E+01	3.54E+01	3.56E+01	3.57E+01
GCI - Av. Temp. [K]	2.03E-02	5.75E-03	1.73E-03	5.76E-04	2.16E-04	-
GCI - Max Temp. [K]	2.67E-03	3.09E-03	5.07E-04	3.86E-04	1.94E-04	-
GCI - ΔP [Pa]	7.09E-02	3.80E-02	1.95E-02	9.88E-03	4.96E-03	-

5. Model of Oregon State University's High Temperature Test Facility

This section presents the development of a Pronghorn model for OSU's HTTF. It is divided into two parts. First, a best estimate model of the steady-state conditions of the facility is constructed. The goal of this step is to validate the modeling approach for simpler conditions than the PG-26 transient. In the second step, the heat up transient before the Depressurized Conduction Cool-down in PG-26 is modeled and compared against experimental measurements.

5.1 HTTF Steady State Conditions.

The model geometry is presented in Figures 7 and 8. The main flow components are the top plenum, top reflector, core, and bottom reflector of the HTTF. Radially, from interior to outside and as depicted in Figure 8, the model contains the blocks of the core (or upper and bottom reflector), the permanent reflector that extents from the top part of the upper reflector to the bottom part of the lower reflector, and the helium gap and core barrel that extend axially across all the flow components. The risers on the outside of the core barrel are not modeled and the flow is assumed to enter directly at the top faces of the the top plenum and helium gap and descend towards the lower plenum. The inlet temperature boundary condition for this model is the measured data by the top plenum thermocouples in the HTTF.

A porous media model is used for the flow components in the top and bottom reflectors and the heated core. Free flow conditions are assumed in the top plenum and helium gap and radiative heat conduction is added to the helium gap. Solid heat conduction is modeled for all components except for the top plenum and the helium gap.

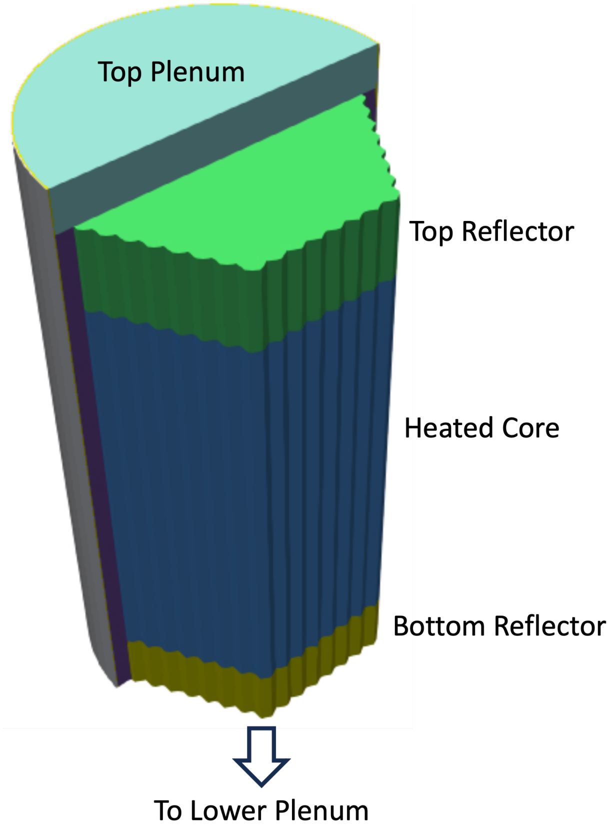

Figure 7: Main flow components modeled in the HTTF.

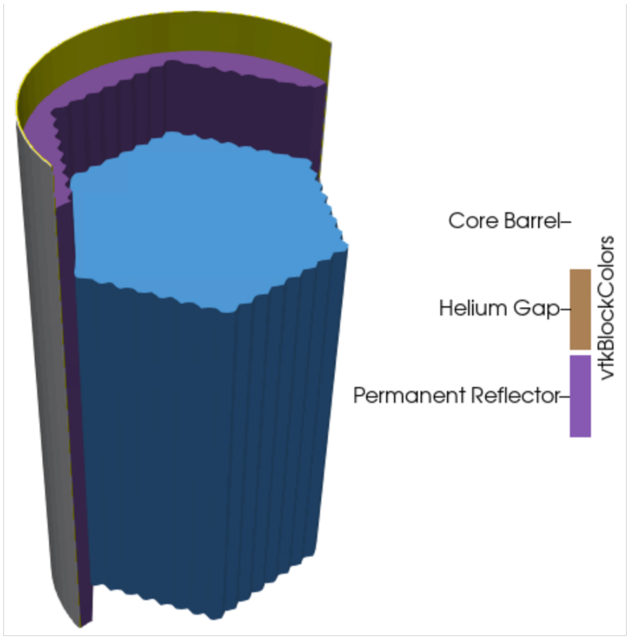

Figure 8: Radial distribution of components modeled in the HTTF.

The core reflectors and inner core of the geometry are divided into hexagonal assemblies. There are 9 types of hexagonal assemblies defined. Even though ring models have previously been used for the HTTF modeling, this hexagonal based model is expected to be more accurate, as it represents the core geometry in a more realistic manner. Ring models average over azimuthal differences in geometry/material, leading to a 1-D radial model, while the hexagonal based approach, retains some of the azimuthal in-homogeneity, thus affording a more realistic 2-D representation, of the the reactor cross-section.

The cross section of the HTTF core blocks and the adopted homogenization approach, is shown in Figure 9. In this figure, cooling channels in the heated region are shown in yellow and heating rods are shown in red. All the heated rods have the same diameter, while the fuel coolant channels are divided into large cooling channels, placed within the heated section, and small and medium diameter cooling channels, which are placed in the boundaries of the heated section (inner and outer respectively). The cooling channels for the central and outer reflector are shown in green.

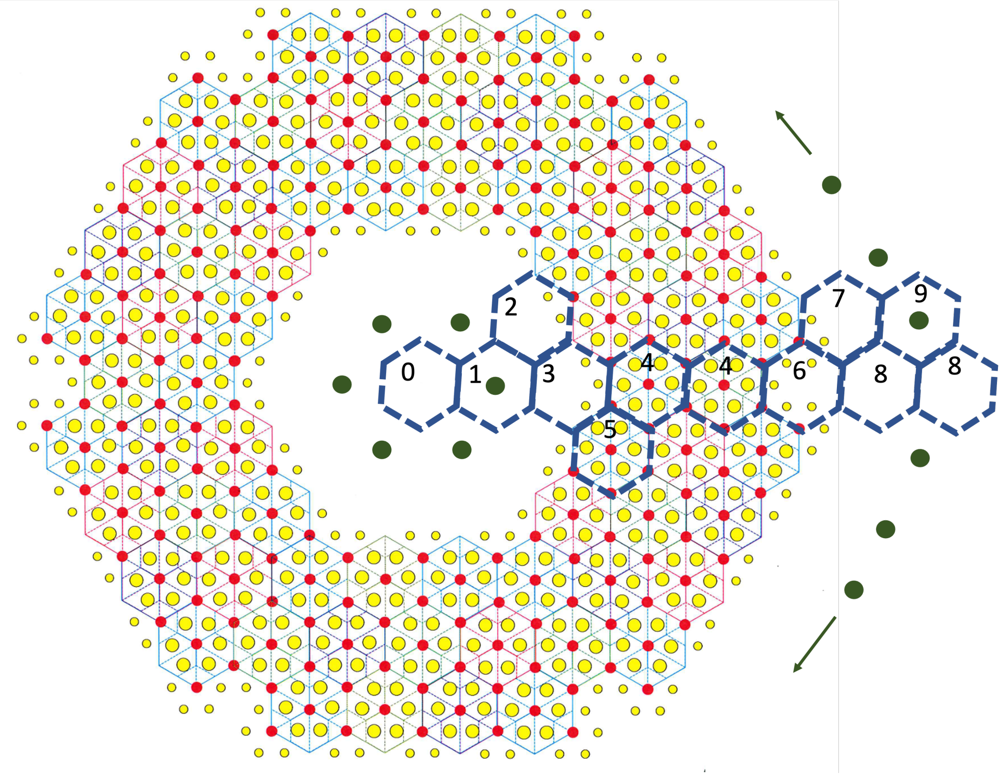

Figure 9: Hexagonal homogenization of the core of the HTTF (adapted from HTTF blueprints).

The 9 hexagonal assemblies defined in this approach, are differentiated according to their unique heating power and effective flow area combination. Note that technically one has only 8 distinct assembles since assemblies 0 and 8 shown in Figure 9 are equivalent. Nonetheless, in the model they are separated on purpose as the phenomena governing the temperature fields those assemblies are very different (i.e., assembly 0 is governed by heat conduction towards the center of the reactor, while assembly's 8 temperature field is regulated by long range heat diffusion from the heated region and cooling by the helium gap). Hence, lumping the assemblies into the same type will introduce errors at the post-processing stage.

The characteristic parameters for each of the 9 hexagonal assemblies is detailed in Table 7. In this table, the flow area, flow perimeter, total area, number of heating rods, and porosity of each assembly is specified. Note that we specified the number of heating rods instead of the volumetric power per assembly in order to be able to automatically adjust the power of the assembly during transient modeling.

Table 7: Details of each of the homogenized assemblies for core blocks of the HTTF.

Index	**Flow Area (m^2)**	**Flow Perimeter (m)**	**Total Area (m^2)**	**Heating Rods**	**Porosity**
0	0	0	5.281e-3	0	-
1	4.909e-4	7.854e-2	5.281e-3	0	9.295e-2
2	1.571e-4	6.283e-2	5.281e-3	3.333e-1	2.975e-2
3	2.356e-4	9.425e-2	5.281e-3	6.667e-1	4.462e-2
4	1.206e-3	3.016e-1	5.281e-3	2	2.284e-1
5	1.206e-3	3.016e-1	5.281e-3	1.833	2.284e-1
6	6.637e-4	2.042e-1	5.281e-3	1.333	1.257e-1
7	2.655e-4	8.168e-2	5.281e-3	3.333e-1	5.027e-2
8	0	0	5.281e-3	0	-
9	2.011e-4	5.027e-2	5.281e-3	0	3.807e-2

The composition of the core region of the HTTF is depicted in Figure 10. The core assemblies are grouped into inner reflector, heated core, and outer reflector.

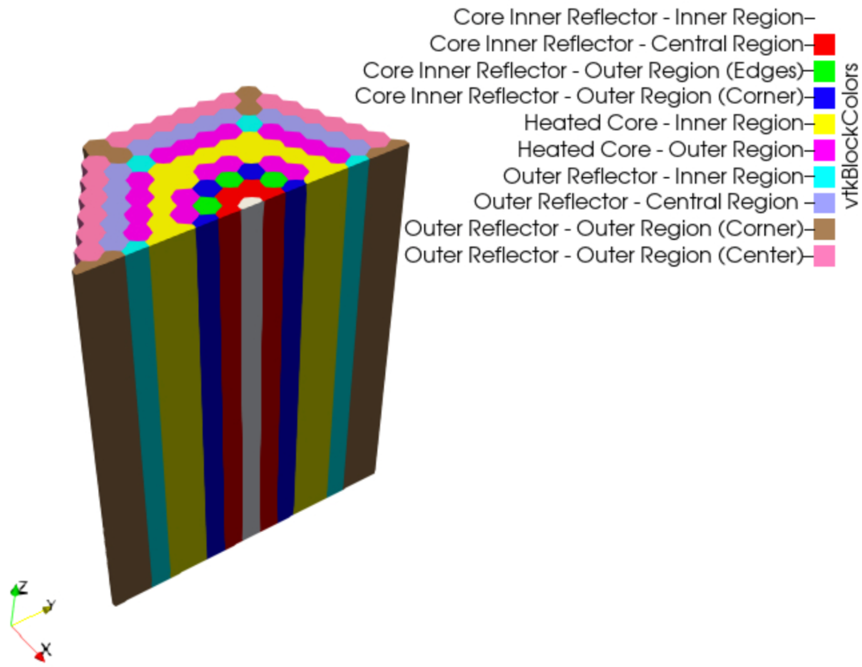

Figure 10: Distribution of homogenized assemblies in the core region of the HTTF.

The porosity field is depicted in Figure 11. The top and bottom reflectors differ from the active core only in that they are not heated. In particular, the top and bottom reflectors have the same porosity as their axial neighbours in the core. The free flow regions at the top plenum and helium gap have a porosity equal to 1. To distinguish top and bottom reflectors from the active core, a separate block structure is used for the blocks in the top and bottom reflector.

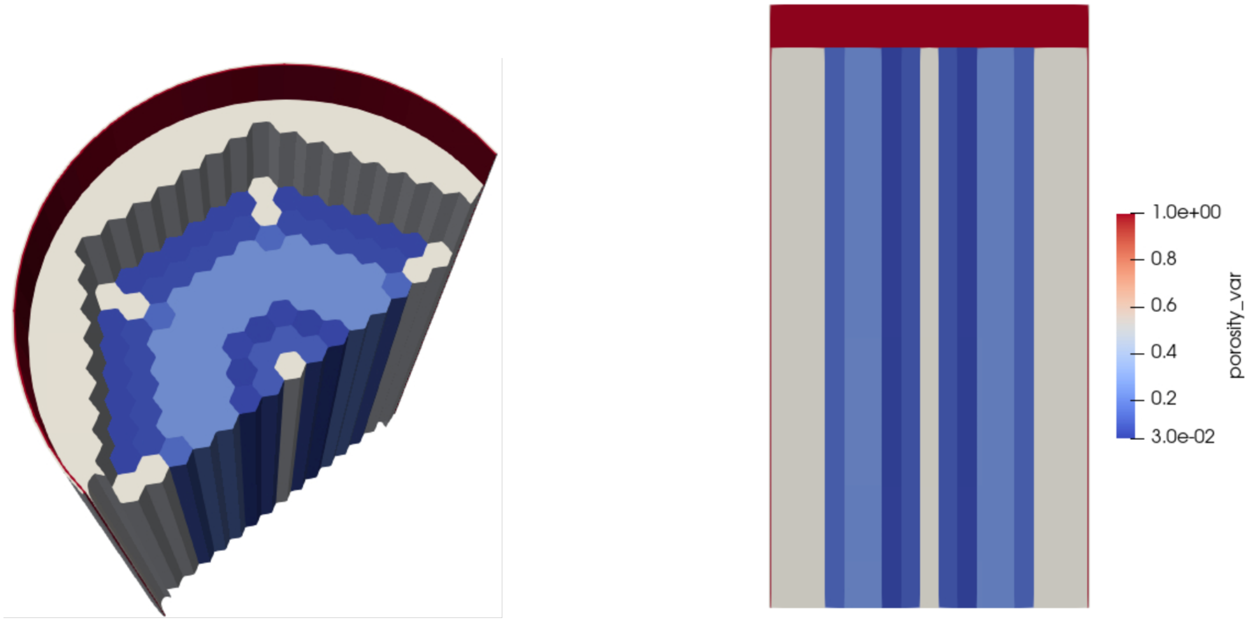

(a) Core Region.

(b) Axial Cut.

Figure 11: Porosity field for the HTTF facility model.

The computational mesh utilized for the HTTF modeling is shown in Figure 12. The hexagons defined in the central reflector, heated core, and outer reflector, are meshed radially with only azimuthal resolution considered (i.e., each hexagon is split into 6 triangles and no additional radial cells are defined). This is because no development of boundary layers is expected in the porous media simulation and hence, a coarse radial mesh is sufficient. The permanent reflector is meshed in the radial direction by a Delaunay triangulation with controlled size to match that of the internal assemblies. The helium gap and core barrel are meshed with regular square elements distributed across the circumference of each component. The helium gap and reactor barrel are discretized radially using two elements. The three-dimensional mesh is obtained by a regular extrusion of the generated two-dimensional radial mesh.

The core is divided axially into 16 sectors, following the findings of the mesh convergence study performed in Section 4. The same discretization length in the axial direction is used for the bottom and top reflectors. As no direct heating is present in those regions, we expect a faster mesh convergence. For the top plenum, the same mesh size in the axial direction is also used. This mesh size is sufficient because the flow is mostly one-dimensional as a uniform inlet flow condition is imposed on the top face. In reality, the upper plenum of the HTTF is subjected to the mixing of flow rising by the external side of the core barrel that turns 180^o to enter the flow channels in the upper reflector. A finer resolution would be required there if the mixing in the top plenum was modeled.

Finally it should be noted, that the heat conduction mesh convergence studies, presented in Section 4.4 exhibited a converged mesh of a coarser discretization, than the one produced for conjugated heat transfer, in Section 4.6. Hence, using the finer axial mesh resolution for the permanent reflector, core barrel and the core region of the HTTF should suffice for both phenomena. Similarly, the fluid flow conditions modeled in Section 4.3 showed a mesh converged at a coarser axial discretization than the conjugated heat transfer problem in Section 4.6. Therefore, using the same finer axial discretization for the helium gap and the core region of the HTTF should also suffice.

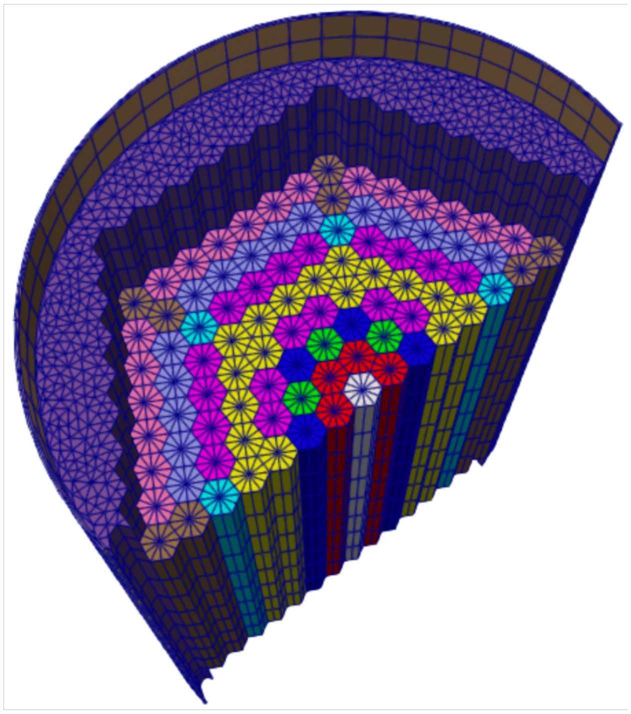

Figure 12: Computational mesh used for the HTTF model.

The following boundary conditions are imposed for the best estimate steady state simulation of the HTTF:

- Inlet Fluid Temperature: 380K,
- Top Solid Fixed Temperature: 380K,

- Inlet Mass Flow Rate: $0.01\frac{\mathrm{kg}}{\mathrm{s}}$,
- Assembly Lateral Walls: No Slip and Conjugated Heat Transfer with the Solid,
- Core Barrel Wall: Free Convection with heat exchange coefficient $h = 10\frac{\mathrm{W}}{\mathrm{m}^2.K}$ and External Free Flow Temperature $T = 380\mathrm{K}$
- Outlet Fluid Temperature: Free Flow,
- Bottom Solid Temperature: Free Convection with Heat Exchange Coefficient $h = 10\frac{\mathrm{W}}{\mathrm{m}^2.K}$ and Free Convection Temperature equals to the Fluid Temperature at the Outlet,
- Outlet Pressure: $200 \times 10^3\mathrm{Pa}$,
- Hydraulic Diameter for Fluid Flow: 0.01m,
- Porosity: 0.1831,
- Power Density per Homogenized Fuel Rod $13655.3\frac{\mathrm{W}}{\mathrm{m}^3}$.

Two items require particular attention. First, the boundary condition for the bottom face of the lower plenum for the solid. In reality, the flow exits from the lower reflector to the bottom plenum of the HTTF, where it mixes and exits towards the IHX. Therefore, the boundary condition for the bottom face of the lower reflector is determined by the convection with the mixing flow temperature of the lower plenum. Second, the power density is reported per homogenized fuel rod. This means that the actual power density of the assembly is determined by the product of the homogenized power density and the number of rods in the assembly reported in Table 7.

Radial and axial cross-sections of the steady-state distributions of superficial and interstitial velocity are depicted in Figure 13. The superficial velocity field shows larger flow cooling at the center of the heated region and the heated part of the core. Examining the interstitial velocity we see that the larger velocities are obtained towards the central reflector, while the rest of the interstitial velocities are approximately uniform for the rest of the assembly.

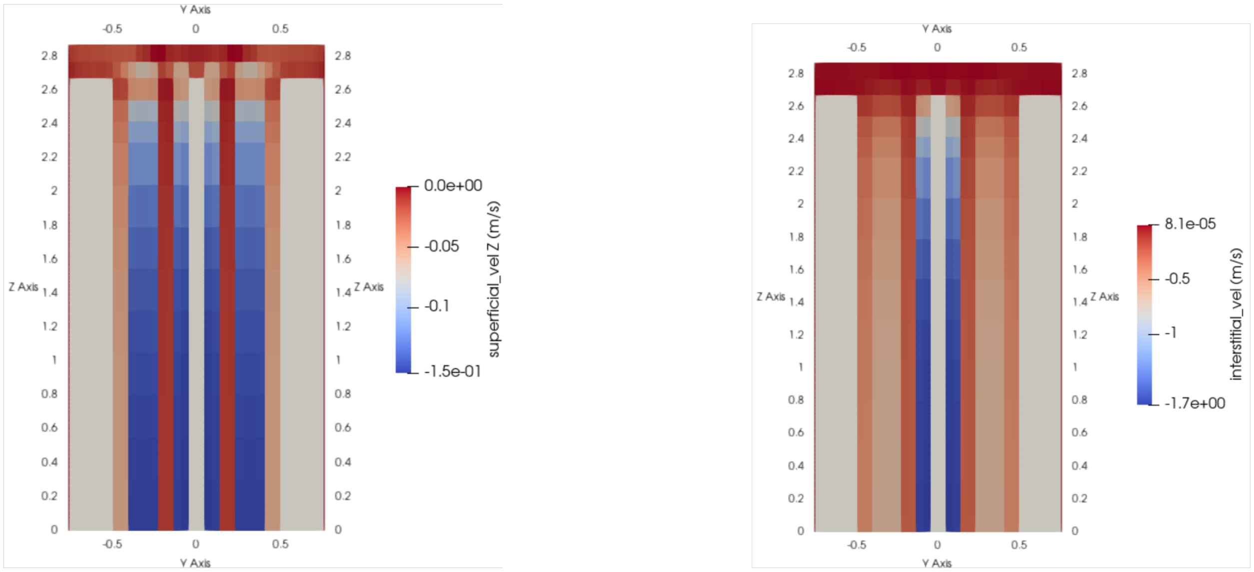

(a) Superficial Velocity - Axial Cut

(b) Interstitial Velocity- Axial Cut

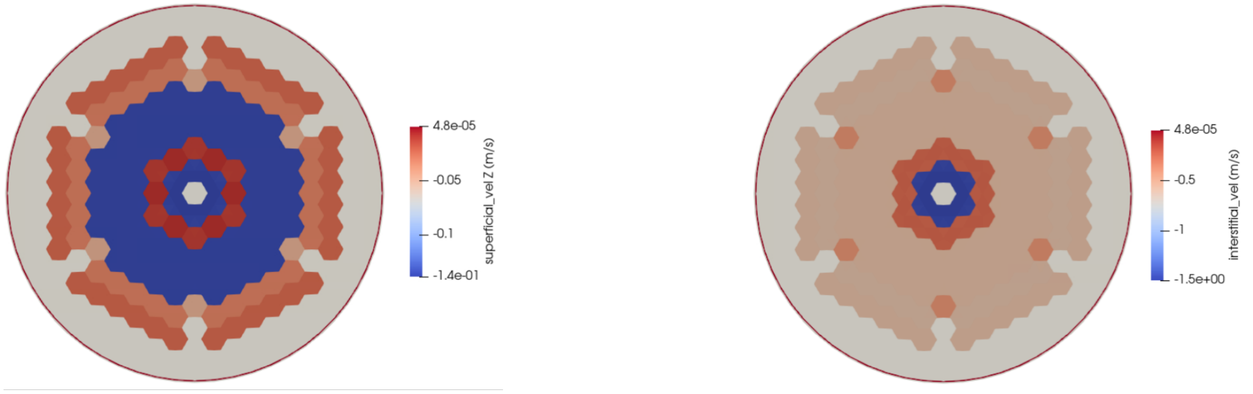

(c) Superficial Velocity - Radial Cut

(d) Interstitial Velocity - Radial Cut

Figure 13: Results for the velocity field in the best-estimate steady-state boundary conditions for the HTTF.

The results obtained for the pressure and the applied power source are presented in Figure 14. The pressure profile is approximately linear from top to bottom. Small differences are exhibited in the pressure radial profile which is almost uniform. This is what is expected for a converged system with uniform porosity in the axial direction. Power is mainly applied in the heated part of the core, with a small amount of power is being deposited in the inner and outer reflectors.

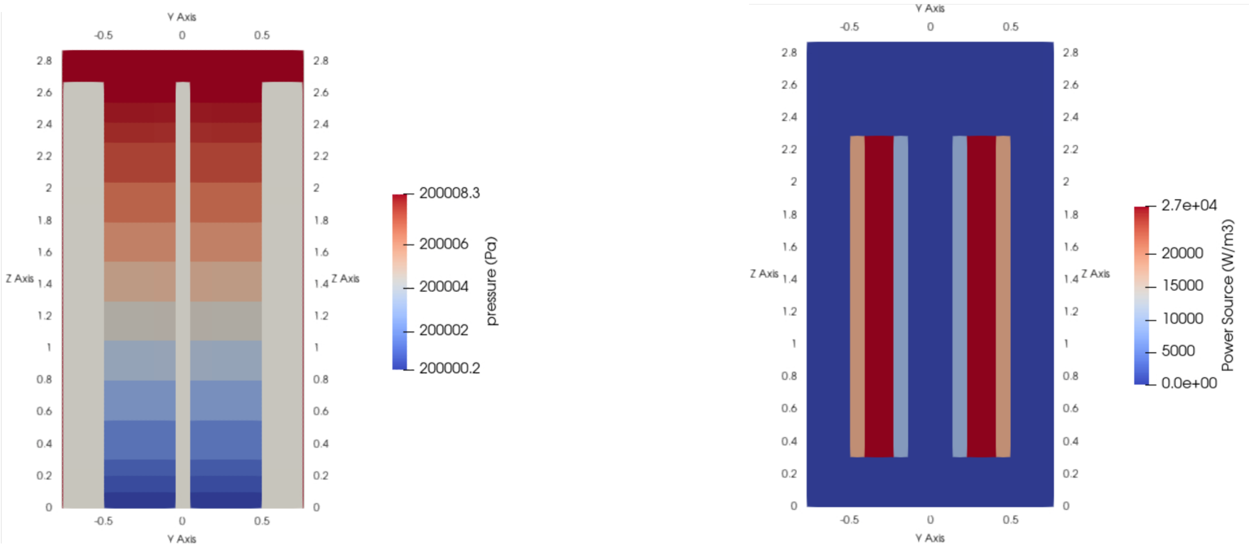

(a) Pressure - Axial Cut

(b) Power Source - Axial Cut

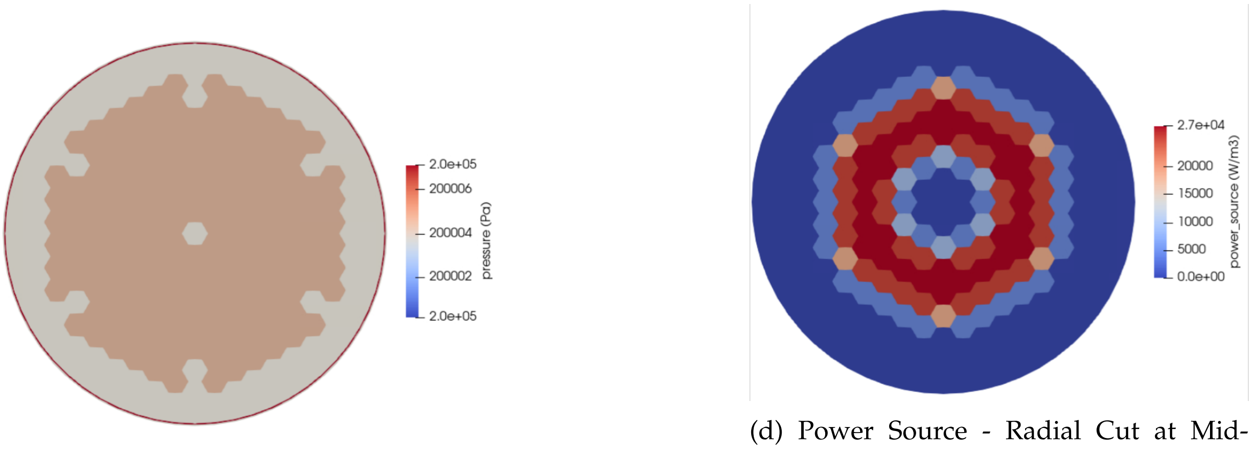

(c) Pressure - Radial Cut at Mid-Height

(d) Power Source - Radial Cut at Mid-Height

Figure 14: Results for the pressure and power source in the best-estimate steady-state boundary conditions for the HTTF.

The three methods for homogenizing the conductivity field in the solid (i.e., average (Eq 12), reciprocal (Eq. 13), and exponential (Eq. 14)) are compared using the temperature profiles obtained for each approach. The results for the fluid and solid temperature fields are shown in Figures 15 and 16, respectively.

Regarding the fluid temperature field shown in Figure 15, as expected the temperature rises in the core region as the coolant flows downwards. The axial temperature profiles are similar, with the maximum temperature rise being at the heated region of the core. However, when we examine the radial profiles, we notice a significantly larger diffusion in the volume average approach that homogenizes the field in the radial direction. For the reciprocal average case, diffusion is much more limited and the heated core region is $\sim 100K$ hotter than the inner and outer reflectors. As expected, due to the mean squared average adopted for the coefficients of the exponential homogenization, the fluid temperature field distribution is not as skewed as the reciprocal average case, but it is less homogeneous than the volume average one.

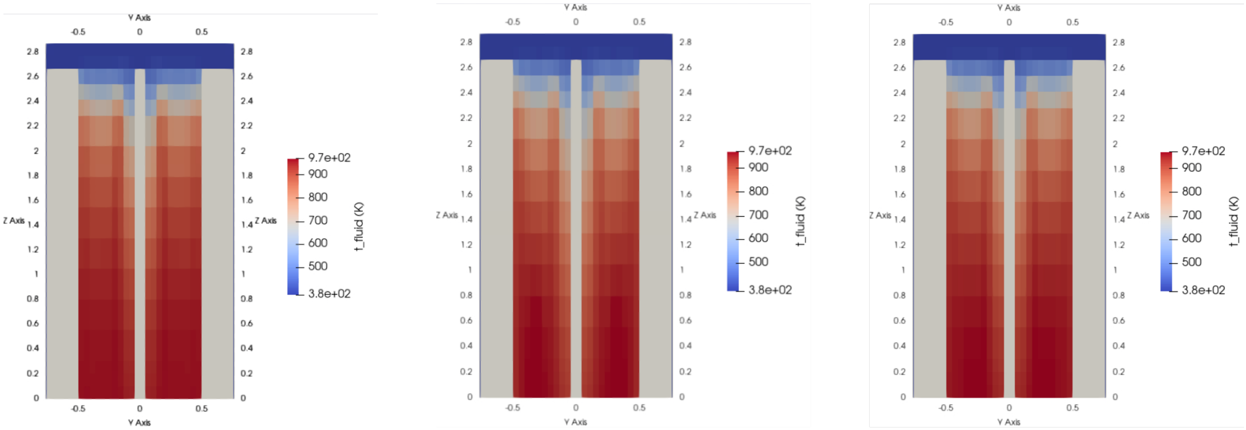

(a) Axial Cut -
Volume Average

(b) Axial Cut -
Reciprocal Average

(c) Axial Cut -
Exponential Average

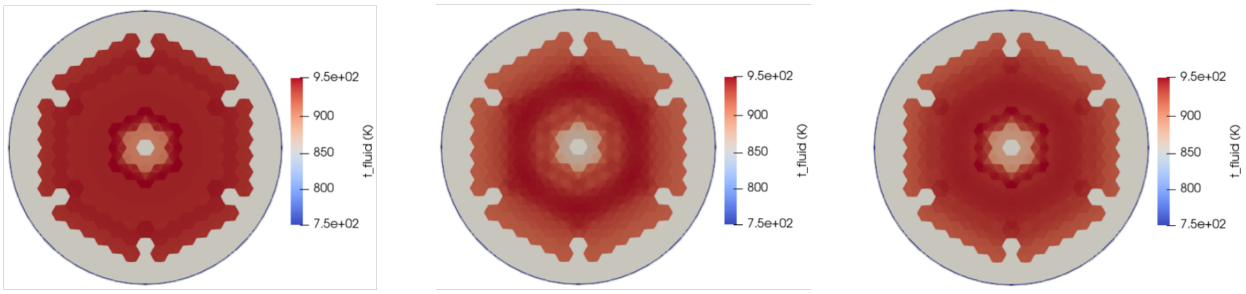

(d) Radial Cut -
Volume Average

(e) Radial Cut -
Reciprocal Average

(f) Radial Cut -
Exponential Average

Figure 15: Results for the fluid temperature profiles for different thermal conductivity homogenization approaches in the best-estimate steady-state model.

A similar conclusion is obtained for the solid temperature field depicted in Figure 16. The temperature field predicted by the volume average approach is highly uniform in both the axial and radial directions due to the high thermal conductivity of the solid block materials in the HTTF. For the reciprocal average, a significant higher temperature is obtained for the heated region of the core. To some extent, heat diffuses to the inner reflector but the outer reflector is colder than the heated fuel region. This is due to the significantly lower effective conductivity predicted by this method. As observed above, in the exponential approach the temperature field obtained is in between the volume and reciprocal averages.

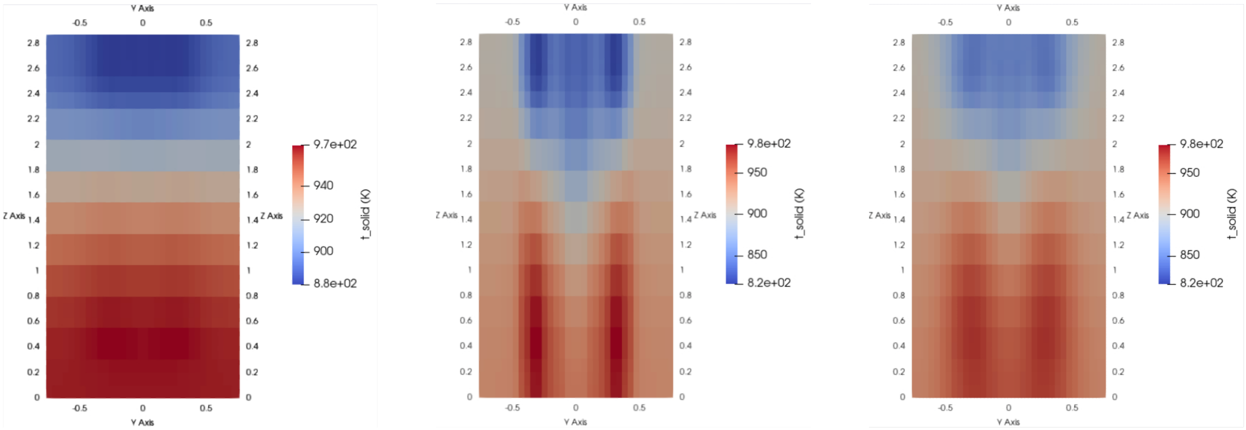

(a) Axial Cut -
Volume Average

(b) Axial Cut -
Reciprocal Average

(c) Axial Cut -
Exponential Average

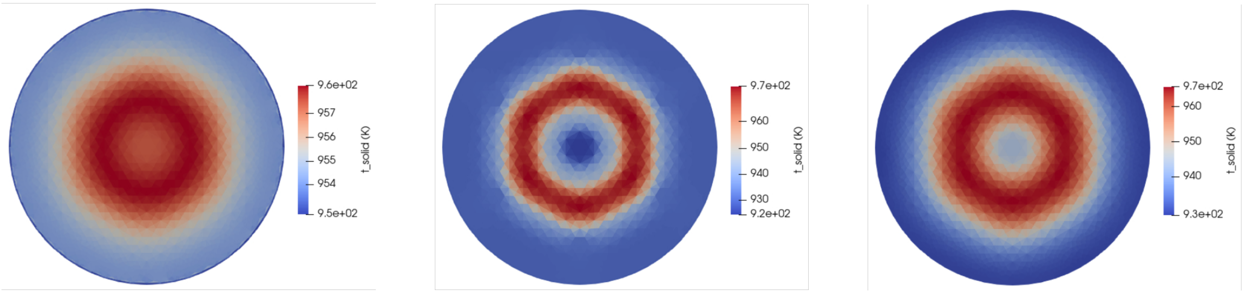

(d) Radial Cut -
Volume Average

(e) Radial Cut -
Reciprocal Average

(f) Radial Cut -
Exponential Average

Figure 16: Results for the solid temperature profiles for different thermal conductivity homogenization approaches in the best-estimate model.

This section demonstrated that the choice of conductivity modeling in the solid region has a significant effect on the temperature distribution in HTTF. Therefore, additional investigation into obtaining accurate averaged thermal properties for application in coarse-mesh thermal-hydraulics models of prismatic HTRs is warranted. It is not possible to further judge these modeling methods without any comparison against experimental data. For this purpose, the heating transient leading to the depressurized loss of coolant (DCC) in test PG-26 is modeled next.

5.2 HTTF Transient prior to PG-26

HTTF has a full design power of 600 kW. For PG-26 only two heated banks were operated, namely 104 and 110. The net power transient leading to the DCC is shown in Figure 17. The power is increased approximately linearly up to the time in which the DCC event is triggered. More details about the PG-26 test can be found in [2].

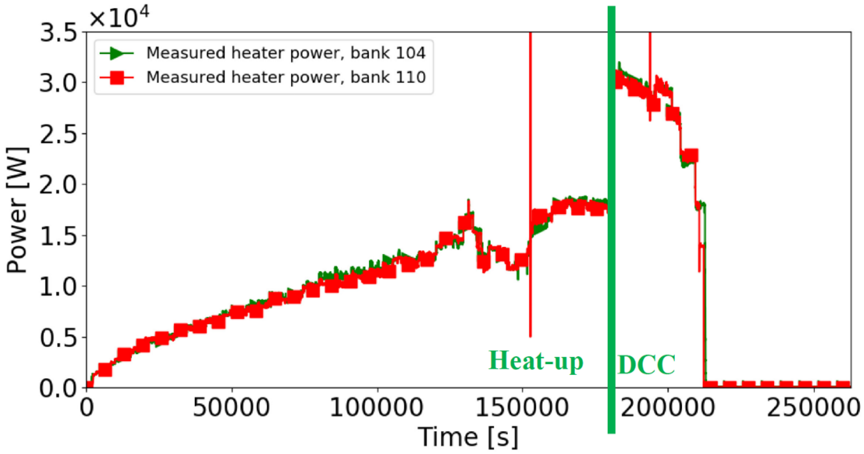

Figure 17: Measured power in heater banks 104 and 110 during the PG-26 transient. Note that the vertical line in the power of bank 110 at 150,000 is an artefact. [2]

The inlet temperature in the top plenum during heating is assumed to be 380K according to the boundary conditions computed by system codes [2]. One of the limitations of the HTTF benchmark, is that inlet flow conditions are not known. Hence, there is not a direct way to impose the mass flux boundary condition at the inlet face of the top plenum. Nevertheless, we can infer the mass flow rate, by requiring the average temperature of helium at the lower plenum, to match that of the experimental measurements at the end of the heating transient. The computed mass flow rate using this approach is $20.65\frac{\mathrm{g}}{\mathrm{s}}$. Note that this methodology is supported by verification exercises 2 and 5, which demonstrate Pronghorn's capability to compute the correct energy balance.

The evolution of the computed helium temperature against the experimental measurement is shown in Figure 18 for all three thermal conductivity averaging cases. Evidently, there are no observable differences since in all cases the imposed power and inlet temperature are the same. In general, good agreement is observed between the computed temperatures and the measured temperatures during the transient. However, a slightly more rapid evolution is observed in the computed temperatures. The reason for this can be non-modeled thermal resistances that prevent the heat from the solid blocks to enter the coolant channels.

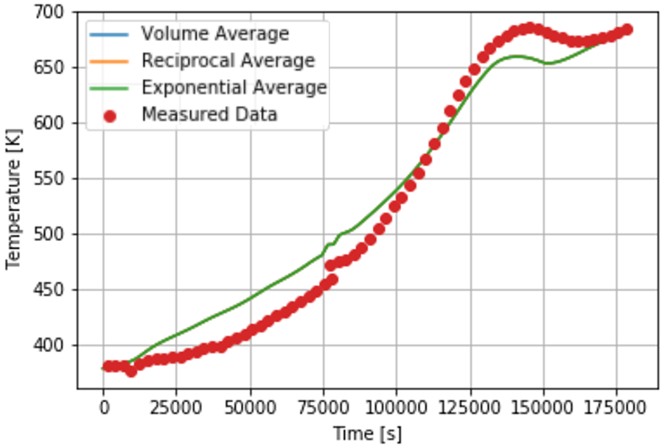

Figure 18: Evolution of the average temperature at the outlet of the lower reflector of the HTTF for the transient leading to the DCC in PG-26.

The rest of the internal conditions, boundary conditions, and material properties for helium and reflectors are equivalent to the ones imposed in Section 5. The evolution of the solid temperature over the core region of the HTTF (i.e., without the top/bottom reflectors and permanent reflector) is shown in Figure 19 for the three thermal conductivity homogenization approaches. Qualitatively, a better result is obtained for the reciprocal average approach than the volume average one. The exponential average approach is between the two. As expected, the thermal conductivity of the volume average approach is too high, which leads to an artificial homogenization of the solid temperatures in the core of the HTTF. On the other hand, the lower effective conductivity predicted with the reciprocal average approach, leads to more heterogeneous temperatures in the core, which match the experimental measurements better. Still, the spread in the average temperatures predicted by the reciprocal average approach is less than the one predicted experimentally. This suggests the presence of thermal resistances, not modeled in current implementation of the porous media modeling.

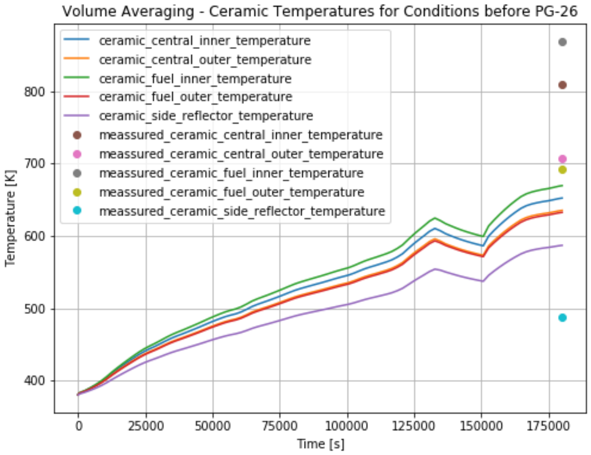

(a) Volume Average.

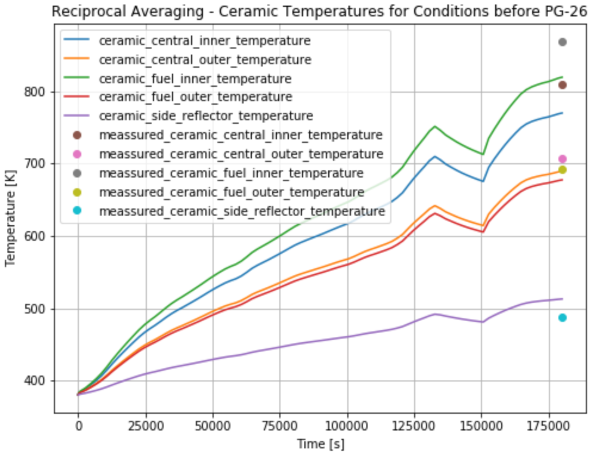

(b) Reciprocal Average.

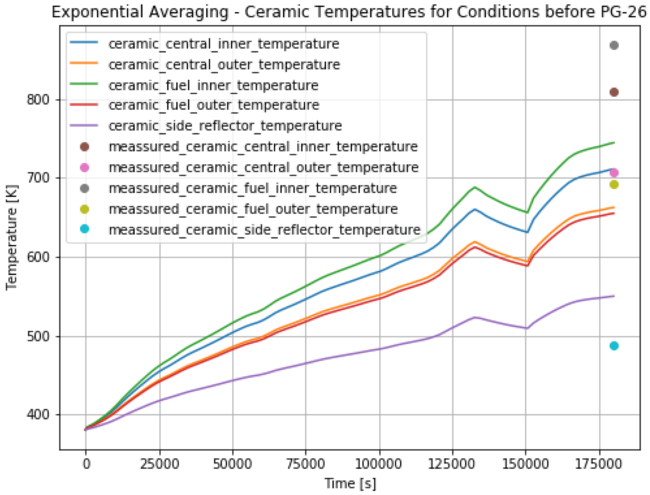

(c) Exponential Average.

Figure 19: Results for the averaged solid temperature evolution for different thermal conductivity homogenization approaches in PG-26.

The relative errors in the average temperature at the end of the heating transient can be defined as follows:

$$T_{error} = \frac{T_{comp} - T_{mean}}{T_{mean} - T_{inlet}}, \tag{31}$$

where T_{comp} is the average temperature computed by the numerical simulation, T_{mean} is the region average of the measured temperatures, and $T_{inlet} = 380K$ is the inlet temperature.

The results obtained for the average temperature errors are presented in Table 8. As expected by observing Figure 19, the reciprocal average approach predicts a significantly smaller error than the other two approaches. The errors predicted with the reciprocal average approach are acceptable for all regions, except for the interior part of the inner reflector. All models predict an over-cooling of the internal part of the inner reflector. This is caused by the over-homogenization of the hexagonal cells located between the central reflector and the heated region (hexagons 2,3), which can be observed by comparing Figures 9 and 7. The distance from the inner portion of the reflector to the coolant channels and in between the coolant channels in that region is quite large. However, in our model these features are homogenized into the hexagonal cell they belong to and act as uniformly distributed heat sinks. These heat sinks when averaged, move closer to the center which leads to an overestimation of cooling. Different modeling approaches will be applied in the future to alleviate this issue.

Table 8: Relative error in the averaged solid temperatures in the regions of interest of the HTTF at the end of the heating of PG-26, previous to the DCC transient.

Region	**Volume Average**	**Reciprocal Average**	**Exponential Average**
Central Reflector - Inner Region	90.2%	24.1%	57.8%
Central Reflector - Outer Region	19.0%	4.2%	11.7%
Heated Core - Inner Region	21.8%	4.9%	13.4%
Heated Core - Outer Region	35.9%	8.9%	22.3%
Outer Reflector	40.4%	10.0%	25.2%

The 3D porous media model has a few advantages when compared with the system code's ring model to model the HTTF facility. First, it allows us to model asymmetric heating. Second, as 3D heat conduction is resolved, there is no need to adjust coefficients for the thermal conductivity. Finally, the homogenization of each assembly does not require the introduction of correction factors to convert the hexagonal shape to a ring geometry.

6. Summary

In this work, the capabilities of Pronghorn to model the prismatic fuel HTR have been examined by developing a porous media flow model of OSU's HTTF. The lack of detailed experimental data on HTRs compelled us to model the HTTF as a surrogate. Due to the complex heat transfer phenomena involved in the HTTF, a series of verification tests was first performed to verify the following regarding Pronghorn's numerical models:

1. Pressure drop in isothermal porous media.
2. Enthalpy balance in porous media with a uniform internal source.
3. Grid convergence for pressure drop in fluid flow phenomena through homogeneous porous media.
4. Grid convergence analysis for heat conduction in porous media.
5. Conjugated heat transfer in porous media.
6. Grid convergence for conjugated heat transfer problems.

The HTTF core was modeled with a series of hexagonal assemblies surrounded by the permanent reflector block. The helium bypass gap and the core barrel were also included. Nine characteristic assemblies were identified and for each assembly, the porosity and effective heating power was computed. The model exhibited qualitatively plausible results for the best-estimate, steady-state conditions of the HTTF. The model was then utilized to simulate the transient heating up of the HTTF facility leading to the PG-26 test. Generally good results were obtained for this comparison when using a reciprocal averaging approach for the solid blocks effective conductivity.

The 3D porous media model has a few advantages when compared with the system codes' ring model to model the HTTF facility. First, it allows us to model asymmetric heating. Second, as 3D heat conduction is resolved, there is no need to adjust coefficients for the thermal conductivity. Finally, the homogenization of each assembly does not require the introduction of correction factors to convert the hexagonal shape to a ring geometry.

This model is still amenable to improvements to reach a stage in which it can be safely used to model HTR phenomena. In particular, the following improvements will be made in successive iterations the model modifications.

- Effective conductivity relations including near-wall effects.
- Better modeling of radiation heat transfer.
- More detailed model of top and bottom plenum mixing.
- Transient and accident modeling.

REFERENCES

[1] B. Woods, “Osu high temperature test facility design technical report, revision 2,” tech. rep., Oregon State Univ., Corvallis, OR (United States), 2019.

[2] A. S. Epiney, “Relap5-3d modeling of high temperature test facility (httf) test pg-26,” tech. rep., Idaho National Lab.(INL), Idaho Falls, ID (United States), 2020.

[3] C. J. Permann, D. R. Gaston, D. Andrš, R. W. Carlsen, F. Kong, A. D. Lindsay, J. M. Miller, J. W. Peterson, A. E. Slaughter, R. H. Stogner, and R. C. Martineau, “MOOSE: Enabling massively parallel multiphysics simulation,” *SoftwareX*, vol. 11, p. 100430, 2020.

[4] A. J. Novak, R. W. Carlsen, S. Schunert, P. Balestra, D. Reger, R. N. Slaybaugh, and R. C. Martineau, “Pronghorn: A multidimensional coarse-mesh application for advanced reactor thermal hydraulics,” *Nuclear Technology*, vol. 207, no. 7, pp. 1015–1046, 2021.

[5] D. R. Gaston, C. J. Permann, J. W. Peterson, A. E. Slaughter, D. Andrš, Y. Wang, M. P. Short, D. M. Perez, M. R. Tonks, J. Ortensi, L. Zou, and R. C. Martineau, “Physics-based multiscale coupling for full core nuclear reactor simulation,” *Annals of Nuclear Energy*, vol. 84, pp. 45–54, 2015.

[6] S. W. Churchill, “Friction-factor equation spans all fluid-flow regimes.,” 1977.

[7] A. Bejan, *Convection heat transfer*. John wiley & sons, 2013.

[8] R. Gajapathy, K. Velusamy, P. Selvaraj, P. Chellapandi, S. Chetal, and T. Sundararajan, “Thermal Hydraulic Investigations of Intermediate Heat Exchanger in a Pool-Type Fast Breeder Reactor,” *Nuclear Engineering and Design*, vol. 238, pp. 1577–1591, 2008.

[9] R. H. Winterton, “Where did the dittus and boelter equation come from?,” *International journal of heat and mass transfer*, vol. 41, no. 4-5, pp. 809–810, 1998.

[10] S. E. Haaland, “Simple and explicit formulas for the friction factor in turbulent pipe flow,” 1983.